Analysis of π^0,η and ω mesons in pp collisions with a high energy photon trigger at ALICE

Satoshi Yano
(M116588)

Quark Physics Laboratory
Department of Physics
Graduate School of Science, Hiroshima University

Supervisor : Prof. Toru Sugitate
Primary examiner : Associate Prof. Kenta Shigaki
Examiner : Associate Prof. Takuya Morozumi

February 20, 2013

Abstract

High energy heavy ion collision is a powerful and unique tool to achieve the high density and temperature like the early universe. At normal temperature, partons are confined in nucleons and they can not move freely due to the asymptotic freedom which is a property of the Quantum Chromo Dynamics (QCD). However, at high density and/or high temperature, they can be deconfined from nucleons. This phase is called the Quark Gluon Plasma (QGP).

Hadron production measurements in proton-proton collisions at the Large Hadron Collider (LHC) energies can observe new phenomena which must be a frontier in the particle physics and allow validation of the predictive power of the QCD and can provide further constrains on pQCD theory for LHC energies. It is well known that the yield of high transvers momentum particles is suppressed in nucleus-nucleus collisions relative to that in proton-proton collisions. This effect is attributed to energy loss of parent partons or perhaps of hadrons after freeze-out.

Since π^0, η and ω consists of only light quarks but different masses, the comparison of the suppression between them can provide systematically information whether the energy loss occurs at the parton level or not. This suppression can be observed at high p_{T} region particles clearly because low p_{T} particles are not only suppression but also recreation from soft processes. So, measurement of high p_{T}particles is suitable to observe this effect. This energy loss measurement requires proton-proton collisions data for base line because this needs to compare between proton-proton and nucleus-nuclear results.

In this thesis, $\pi^0$and η mesons are observed via 2 photons decay channel and ω is measured via 3π decay channel in proton-proton collisions at $\sqrt{s} = 8$TeV. We use the Photon Spectrometer to measure photons and the Time Projection Chamber to measure charged tracks. We analyze high energy photon trigger data to measure higher p_{T} mesons than the minimum bias data. This high energy photon trigger can measure selectively high energy photon events. This trigger is fired by a cluster has above threshold discriminated by the Trigger Region Unit (TRU). The method of analyzing this trigger data had not been established by anybody. However, I have done it and measured neutral mesons spectra in proton-proton collisions at $\sqrt{s} = 8$TeV for the first time in the world.

Contents

1 Introduction

1.1 Standard Model

At all times one of mysteries is the composition of everything. Today the best answer lies in the Standard Model of particle physics which introduced the basic particles, forces and rulrs of their combinations and interactions. According to the Standard Model everything in the world consists of leptons and quarks.

Four interactions (forces) exist, Electromagnetic interaction, Weak interaction, Strong interaction and Gravity. Each interactions have steady medium particles. The medium particles are called Gage Boson. Gage boson of electromagnetic interaction is photon (γ). Weak interaction gage boson is called weak boson. There are three different types of weak boson. One is Z boson and this is neutral particle and the others have electric charged weak boson (W^+, W^-). The strong interaction gage boson is gluon (g). Strong interaction acts between particles which have color charge. The last interaction is gravity and its gage boson is called graviton. However, it has not been observed yet, so it is theoretical particle. The gravity is not included in the Standard Model. Following tables show you summary of them.

	u	d	s
Q *-electric charge*	$+\frac{2}{3}$	$-\frac{1}{3}$	$+\frac{2}{3}$
J *-spin*	$\frac{1}{2}$	$\frac{1}{2}$	$\frac{1}{2}$
I_Z *-isospin*	$+\frac{1}{2}$	$-\frac{1}{2}$	*0*
S *-strangeness*	*0*	*0*	*-1*
C *-charm*	*0*	*0*	*0*
B *-beauty*	*0*	*0*	*0*
T *-topness*	*0*	*0*	*0*
mass (MeV/c^2)	*1.5-3.0*	*3.0-7.0*	*95±25*

	c	b	t
Q *-electric charge*	$+\frac{2}{3}$	$-\frac{1}{3}$	$+\frac{2}{3}$
J *-spin*	$\frac{1}{2}$	$\frac{1}{2}$	$\frac{1}{2}$
I_Z *-isospin*	*0*	*0*	*0*
S *-strangeness*	*0*	*0*	*0*
C *-charm*	*1*	*0*	*0*
B *-beauty*	*0*	*1*	*0*
T *-topness*	*0*	*0*	*1*
mass (GeV/c^2)	*1.25±0.09*	*4.20±0.07*	*174.2±3.3*

	γ	W^+	W^-	Z	g
Q -electric charge	*0*	*+1*	*-1*	*0*	*0*
J -spin	*1*	*1*	*1*	*1*	*1*
Relative strength	10^{-2}	10^{-13}	10^{-13}	10^{-13}	*1*

1.1.1 Quantum Chromodynamics (QCD)

The Standard Model includes the basic interactions between particles and consists of Quantum Electro-Weak Dynamics (QED) and Quantum ChromoDynamics (QCD). The QED describes weak and electromagnetic interactions. Strong interactions is described by QCD.

The QCD was developed as an extension of QED via the imposition of a local SU(3) symmetry in color space and based on the gage field theory. The QCD describes interactions between quarks and gluons. The Quarks have 6 flavors and have 3 colors while the gluons have 8 colors but not have flavors. The classical QCD Lagrangian is

$$L_{QCD} = -\frac{1}{4}F^{\alpha}_{\mu\nu}F^{\mu\nu}_{\alpha} + \bar{\alpha}(i\gamma^{\mu}D_{\nu} - \mathbf{M})\mathrm{q} \tag{1}$$

where D_{μ} is a covariant derivative defined as

$$D_{\mu} \equiv \partial_{\mu} + ig_s t^a A^a_{\mu} \tag{2}$$

The $F^a_{\mu\nu}$ is the field tensors of the gluon given by

$$F^a_{\mu\nu} = \partial_{\mu}A^a_{\nu} - \partial_{\nu}A^a_{\mu} - g_s f_{abc}A^b_{\mu}A^c_{\nu} \tag{3}$$

the A^a_{μ} is the gluon gage field, g_s is the QCD coupling constant, γ^{μ} are Dirac matrices and defined as $|\gamma^{\mu}\gamma^{\nu} + \gamma^{\nu}\gamma^{\mu} = 2g^{\mu\nu}$, and f_{abc} is the structure constant of the SU(3) and the $\mathbf{M}$ is the diagonal matrix of current quark masses.

The most important difference between the QCD and the QED is that the QCD is the non-abelian gauge theory and has gluon self-interaction as a consequence. This nature of the QCD leads asymptotic freedom relevant to the quark confinement. The strong coupling constant α_s can be expressed as a function of the momentum transfer Q^2 as follows

$$\alpha_s(Q^2) \sim \frac{12\pi}{(33 - 2N_f)ln(Q^2/\lambda^2_{QCD})} \tag{4}$$

where N_f is the number of quark flavors and $\lambda_{QCD} \sim 0.2$ GeV is the typical QCD scale. When the momentum transfer Q^2 is much larger than λ^2 QCD, α_s becomes small enough to allow us to use the perturbative method for the QCD calculation (pQCD) as is the case in the QED. On the other hand, when the momentum transfer Q^2 is not large, the QCD is in non-perturbative regime and many approaches have been proposed to compute the non-perturbative effect.

1.1.2 Quark Gluon Plasma (QGP)

The color confinement may be broken with increase of the temperature and density of many body system consisted of hadrons. This results in a phase transition from the confined nuclear matter (ordered phase) to the deconfined state (disordered phase). The deconfined state is called Quark Gluon Plasma (QGP).

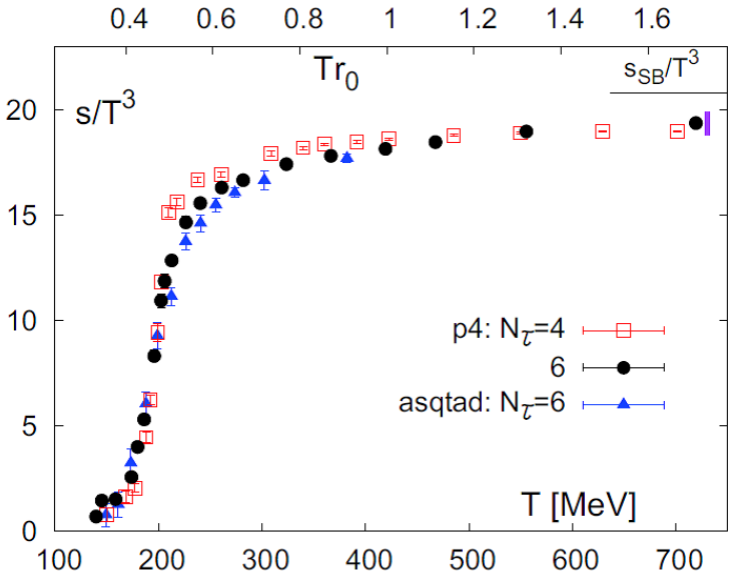

Figure 1: The entropy density ($s = \epsilon + p$) in units of s/T^3 as a function of T calcilated with lattice QCD[7]

The lattice QCD calculations predict that the phase transition to the QGP state occurs at a critical temperature, T_c, of 150-200MeV. Fig.1 shows the calculated results of the entropy density s/T_c as a function of temperature T. The entropy density increases in stepwise at $T_c \sim 200$ MeV due to the increase of the degree of freedom, which is associated by the deconfinement of the matter. A schematic phase diagram of hadronic matter including the QGP is shown in Fig.2 The horizontal axis is the baryon density normalized to the density of the normal nuclear matter ($\sim 0.15\mathrm{GeV/fm}^3$) and the vertical axis is the temperature. The QGP is considered to have existed in high temperature circumstances of the early universe, a few micro second after the Big Bang.

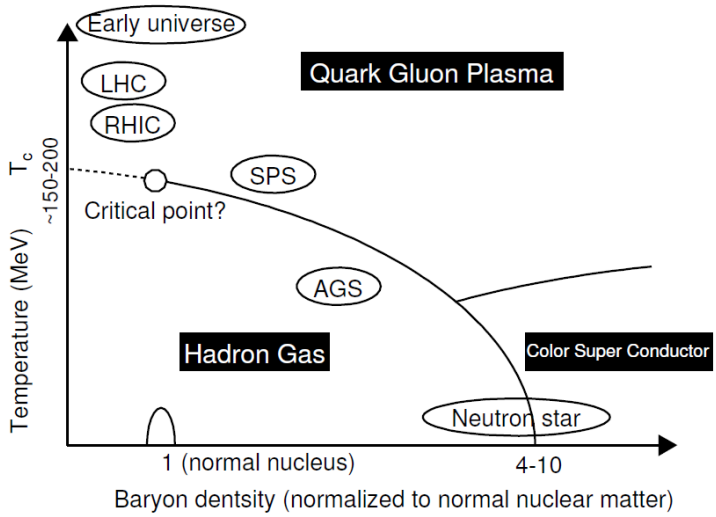

Figure 2: A schematic phase diagram of QCD matter

1.2 Heavy Ion Collision

1.2.1 The pQCD in Heavy Ion Collision

Many previous experiments did $p+p$, $p+\bar{p}$ and $A+A$ collisions and excellent results were observed.

The hard scattering process of two hadrons collision at high energy is given as interaction of quarks and gluons which are in the initial hadrons. The cross section of the hadron production for a hard scattering process in $p+p$ collision is given by

$$\begin{aligned}\sigma^{pp\to hX} = \sum_{f_1,f_2,f} \int dx_1 dx_2 dz \dot{f}_1^p(x_1,\mu^2)\dot{f}_2^p(x_2,\mu^2) \\ \times\sigma^{f_1 f_2\to fX}(x_1p_1, x_2p_2, p_h, \mu) \times D_f^h(z,\mu^2)\end{aligned} \tag{5}$$

The μ is the facrization scale,f_1, f_2, f are partons, $f_1^p(x_1,\mu)$ and $f_2^p(x_2,\mu)$ are parton distribution function (PDF) of parton incoming 1st and 2nd protons respectively. $D_f^h(z_h,\mu^2)$ is fragmentation function (FF) from parton f to hadron h, p_1 and p_2 are the momentum of initial protons.

The Parton Distribution Function (PDF)

A proton consists of up, up and down quarks as valence quark. However, there are not only valence quarks. Gluons connect quarks and the other quarks and can connect gluons themselves in a proton.

Gluon can emit gluons and then these gluons can create a quark and anti-quark pair. The quark pair can recombine and create a gluon. Quarks and gluons are reiterate creation and annihilation in a proton. These quarks which are created and annihilate in a proton are called sea quarks.

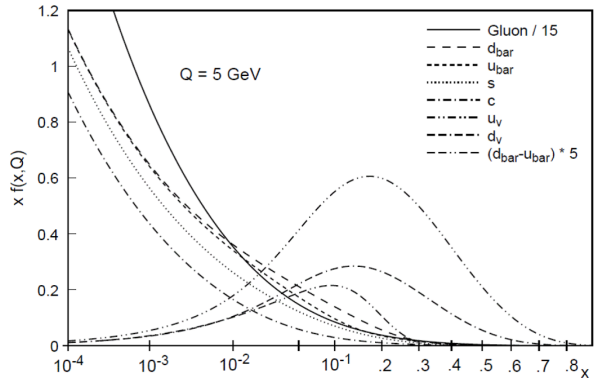

Figure 3: Parton Distribution Function as a function of x at $Q = 5\text{GeV}$[15].

As mention above, there are not only 3 quarks in a proton. The parton distribution function is the probability density for each valence and sea quarks and gluons. The PDF as a function of x is shown in Fig.3. The vertical axis is probability density and the horizontal axis is x. The x is called the Bjorken x and this is defined as

$$x = E'/E \tag{6}$$

where E' is parton energy and E is proton energy. The PDF is tried to extract from experimental data by several theoretical groups. Fig.3 is based on the next-to-leading-order (NLO) pQCD calculation.

The Fragmentation Function (FF)

The Fragmentation Function, $D_i^h(z, Q^2)$, encodes the probability that the parton i fragments into a hadron h carrying a fraction z of the parton's momentum. The quark-parton-model constrains such as the momentum sum rule

$$\sum_h \int_0^1 dz z D_i^h(z, \mu^2) = 1 \tag{7}$$

The dependence of the D_i^h on the factorization (or fragmentation) scale μ^2.

1.2.2 Collision scenarios

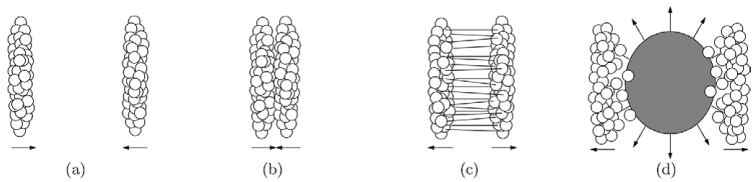

Figure 4: A heavy ion collision with transparency (Bjorken picture)[2].

Fig.4 describes a heavy ion collision in the Bjorken model. In this model the nuclei interpenetrate each other losing their energy. Bjorken models stands on following assumptions :
1)The collisions are transparent in the sense that the region around $y = 0$ is net-baryon free, 2)the number of produced particles per unit rapidity,dN/dy, is assumed to be constant within a few units of rapidity around $y = 0$, 3) at a time $\tau \sim 1\text{fm}/c$ the matter in the fireball is thermalized and relativistic hydrodynamics is applicable to describe the expanding fluid, 4) for central collisions transverse expansion can be ignored for a time compareble to the size of the nuclei divide by c. This reduces the problem of describing the collisions to a two-dimensional one in z and τ.

1.2.3 Glauber Calculation

It is possible to estimate geometrical properties of the heavy ion collision with Glauber Model[18]. This model requires two inputs from physics data.

One is nuclear charge density. This is given by

$$\rho(r) = \rho_0 \frac{1 + w(r/R)^2}{1 + exp(\frac{r-R}{a})} \tag{8}$$

where ρ_0 is the density of the nucleus, R is the radius of the nuclear, a is the 'skin depth' of the nuclear and w is the deviation of a spherical shape of the nuclear.

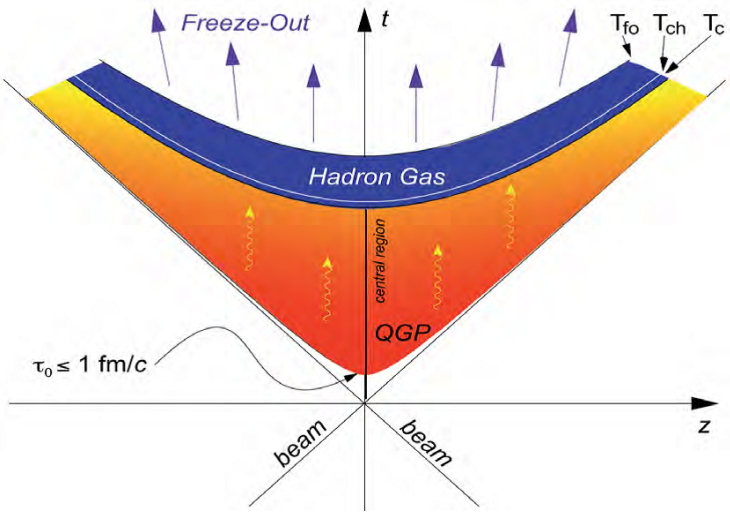

Figure 5: The Bjorken space time diagram. The (z,t) hyperoblas mark the boundaries between the difference phases[2].

The other one is inelastic nucleon-nucleon cross section σ_{inel}^{NN}. To estimate the individual nucleon-nucleon interactions in heavy ion collisions are needed to simulate collisions.

In this calculation, the number of collisions between individual collisions N_{coll} can be calculated as a function of impact parameter b as following

$$N_{coll}(b) = \sum_{n=1}^{AB} nP(n,b) = AB\hat{T}_{AB}(c)\sigma_{inel}^{NN} \tag{9}$$

$$\hat{T}_{AB}(b) = \int \hat{T}_A(s)\hat{T}_B(s-b)d^2s \tag{10}$$

where $\hat{T}_{AB}$ is the thickness function of overlap of A and B. The number of participant N_{part} can be determined as below

$$N_{part}(b) = A\int \hat{T}_A(s)\{1-(1-\hat{T}_B(s-b)\sigma_{inel}^{N}N)^B\}d^2s$$
$$+B\int \hat{T}_B(s-b)\{1-(1-\hat{T}_A(s)\sigma_{inel}^{NN})^A\}d^2s \tag{11}$$

N_{part} and N_{coll} are important parameters to analyze heavy ion collisions.

1.3 High p_{T} Suppression

1.3.1 Energy Loss in the medium

A phenomenon that a yield of high p_{T} particle in nucleus-nucleus collisions is smaller than that of proton-proton collisions has been observed in previous experiments. For example, Fig.6 is the PHENIX result and shows that high p_{T} hadrons are suppressed, but direct photon is not. It is translated into a energy loss of parent par-

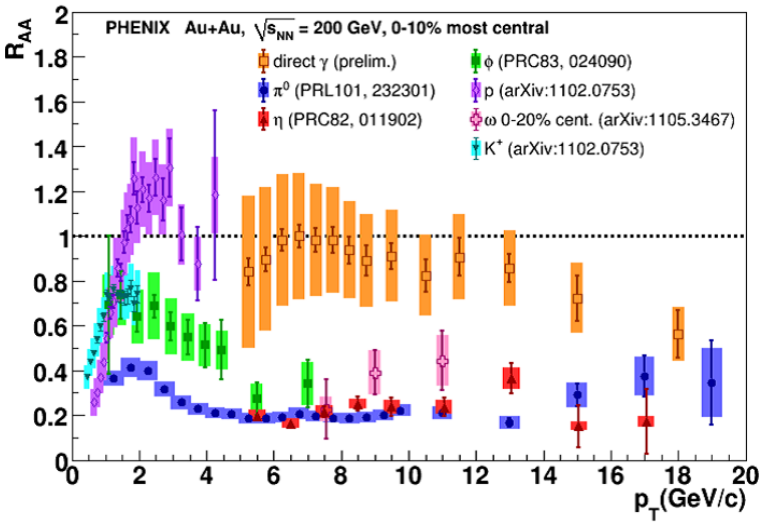

Figure 6: The R_{AA} result of the PHEINX

tons or perhaps of hadrons in a medium created by nucleus-nucleus collisions.

This effect can be evaluated quantitatively with the nuclear modification factor

$$R_{AB}(p_{\mathrm{T}}) = \frac{d^2N_{AB}/dydp_{\mathrm{T}}}{(< N_{coll} > /\sigma_{pp}^{inel}) \times d^2\sigma_{pp}/dydp_{\mathrm{T}}} \tag{12}$$

where N_{coll} is the number of binary nucleous-nucleus collisions depending on the impact parameter range of corresponding centrality, $d^2N_{AB}/dydp_{\mathrm{T}}$ is the invariant yield per unit rapidity, σ_{pp}^{inel} and $d^2\sigma_{pp}/dydp_{\mathrm{T}}$ are the total and differential cross section for inelastic proton-proton collisions respectively. In the absence of matter effect, this R_{AB} should be $R_{AB} = 1$ at a high p_{T}. Inversely, if R_{AB} is lower

than 1, the yield of nucleus-nucleus collisions is smaller than that of scaled proton-proton collisions. This result implies the matter is created by collisions.

1.4 Motivation

The LHC has been running since 2009 and now the collision energy achieves 8TeV. This is energy frontier for collider experiments. This thesis is the first 8 TeV proton-proton collisions analysis in the ALICE. The ALICE has many high level trigger criteria to cover wide physics topics. I analyzed the PHOS triggered data which is specialization to detect high energy photons. Actually, the method of analyzing this triggered data was not established. One goal of this thesis is to establish the method.

The high p_{T} suppression has been observed at the LHC and the RHIC experiments[10]. This effect is attributed to energy loss of parent partons or perhaps of hadrons after freeze-out. Since π^0, η and ω consists of only light quarks but different masses, the comparison of the suppression between them can provide systematically information whether the energy loss occurs at the parton level or not. This suppression can be observed at high p_{T} region particles clearly because low p_{T} particles are not only suppression but also recreation from soft processes. So, measurement of high p_{T} particles is suitable to observe this effect. This energy loss measurement requires proton-proton collisions data for base line. The proton-proton collisions results can be base line for many nucleus-nucleus and/or proton-nucleus results and so on. Therefore, this thesis encloses very important results.

2 Experimental Setup

2.1 The Large Hadron Collider

The Large Hadron Collider (LHC) was constructed between 2002 and 2009 at the CERN laboratory. It is the largest and most powerful particle accelerator ever built. It was installed in the 27 km long circular underground tunnel and that hosted its predecessor the Large Electron Positron (LEP). 16 radio-frequency (RF) accelerating cavities and over 1600 superconducting magnets allow it presently to accelerate, store and collide protons and leads with a centre of mass energy and center of mass energy per nuclear up to 14 TeV and 5.5 TeV respectively. The number of dipole magnets about 10000 and their operating temperature is 1.9K.

The main objectives are looking for the higgs boson which are predicted by SM and, beyond SM, the SUSY and the dark matter. In 2010 and 2011, the luminosity was $2 \times 10^{32} cm^{-2} s^{-1}$.

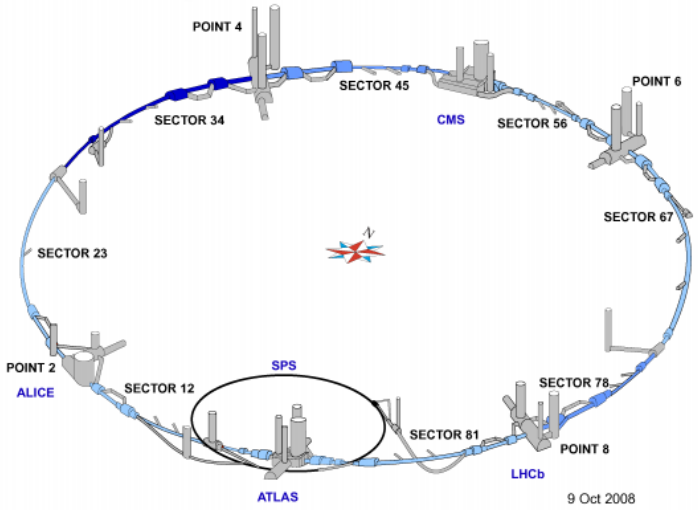

Figure 7: The LHC layout

2.2 The ALICE Detector

A Large Ion Collider Experiment (ALICE) is a large experiment placed at one of the four collision points of LHC. The collaboration

involves about 1200 scientists and engineers from 116 institutes in 33 countries. It was designed to study the properties of QCD and to characterize the Quark-Gluon Plasma (QGP). It is the only experiment at LHC which was optimized for the heavy ions collisions. Detectors in the the ALICE are designed to measure many physics phenomena which are observed at RHIC.

The detector is placed in the solenoid magnet from the old LEP experiment. This provides a relatively low magnetic field of 0.5 T, which allows to measure with high performance low momentum particles corresponding to the so-called soft QCD, as well as more energetic particles form hard processes.

Its overall dimensions are $16 \times 16 \times 26\text{m}^3$ with a total weight of approximately 10 000 t. The ALICE detectors consist of a central barrel part, which measures hadrons, electrons, and photons, and a forward muon spectrometer.

Because of the extremely high multiplicity expected in central nucleus-nucleus collisions at LHC energies, the design of the ALICE detectors are optimized for measurement under high multiplicity ($dN_{ch}/dy = 8000$) environment. ALICE has an efficient and robust tracking system over a large momentum range, from tens of MeV/c (soft physics) to over 100 GeV/c (jet physics). A specificity of the ALICE detector over the other LHC experiments is its large focus on hadron and lepton identification (PID). It is achieved over much of the momentum range using most known PID techniques: specific ionization energy loss.

2.2.1 Central Detector

Inner Tracking System (ITS)

The Inner Tracking System (ITS) consists of six cylindrical layres of silicon detectors , located at radii between 4 and 43cm. It covers the rapidity range of $|\eta| < 0.9$ for all verrices located within the length of the interaction diamond. The main tasks of the ITS are to localize the primary vertex with a resolution better than 100μm, to reconstruct the secondary vertices from the decays of hyperons and D and B mesons, to track and identify particles with momentum below 200MeV/c and to improve the momentum and angle resolution for particles reconstructed by the Time-Projection-Chamber.

The two innermost layers, Silicon Pixel Detector (SPD), are based on hybrid silicon pixels. The first layer and second layer are palced

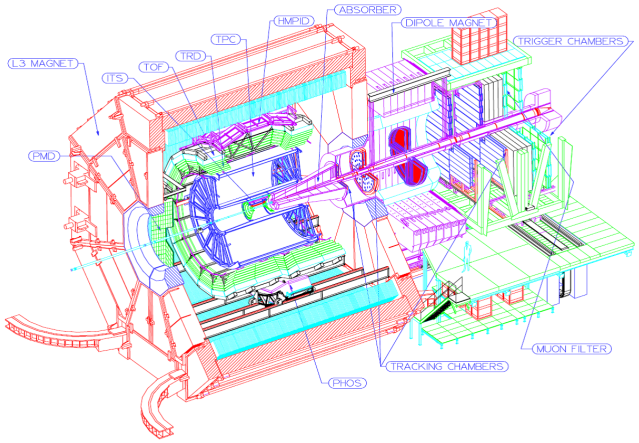

Figure 8: The over view of ALICE detector[1]

at 3.9 and 7.6 cm from interaction point and rapidity and cover in rapidity range $|\eta| < 2.0$ and $|\eta| < 1.4$ respectively. The SPD has about 9.8 million channels.

The third and fourth layer are Silicon Drift Detector (SDD) and consist of a 200μm thick sillicon. The SDD can measure the energy loss of a charged particle to identify the particle. The SDD has 133,000 channels.

The two outermost layers are Silicon Strip Detector (SSD) which consist of sensors equipped on both side with silicon micro strip. It can measure track position and enery loss for particle identification. The SSD has approximately 2.6 million channels.

Time projection Chamber (TPC)

The Time-Projection Chamber (TPC) is the main tracking detector of the central barrel and is optimized to provide, together with the other central barrel detectors, charged particle momentum measurements with good two track separation, particle identification, vertex determination. The phase space covered by the TPC in rapidity is $|\eta| < 0.9$ and full azimuth. The TPC is a large volume ($88m^3$) and it is suffused with mixed gas ($Ne/CO_2/N_2$). At lage p_T range is covered from low p_T of about 0.1GeV/c up to 100GeV/c with good momentum resolution. It is designed as that dE/dx resolution better than 5%, a relative p_T resolution better than 1% for momenta

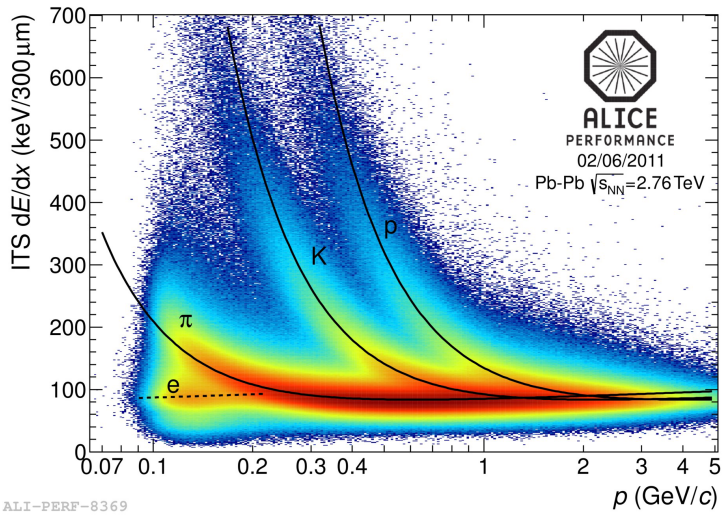

Figure 9: The ITS dEdx picture[1]

of 1 GeV/c and better than 2.5% for momenta of 4GeV/c and two track resolution enable us to separate tracks with a relative momentaum difference of < 5MeV.

Time of Flight (TOF)
The Time-Of-Flight detector covers the central region ($|\eta| < 0.9$, full azimuth). It can identify in the intermidiate momentum range, below 2.5GeV/c pions and kaons, up to 4GeV/c for protons. TOF can measure times with good resolution about tens of pico seconds. To identify particles, their momentum are needed to calculate their mass. So, particle tracks measured by ITS and TPC are extended to TOF position.

Transition Radiation Detector (TRD)
The main purpose of Transition Radiation Detector (TRD) is to provide electron identification in the central barrel for momentum above 1GeV/c. Below this momentum electrons can be identified via specific energy loss measurement in the TPC. Its pion rejection factor is 100 for over 1GeV/c. The methods of electron identification are utillizing specific energy loss and transition radiation.

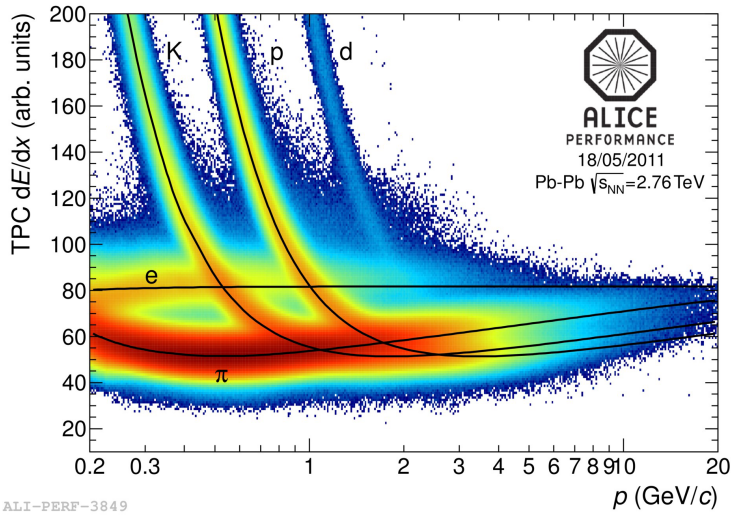

Figure 10: The TPC dEdx picture[1]

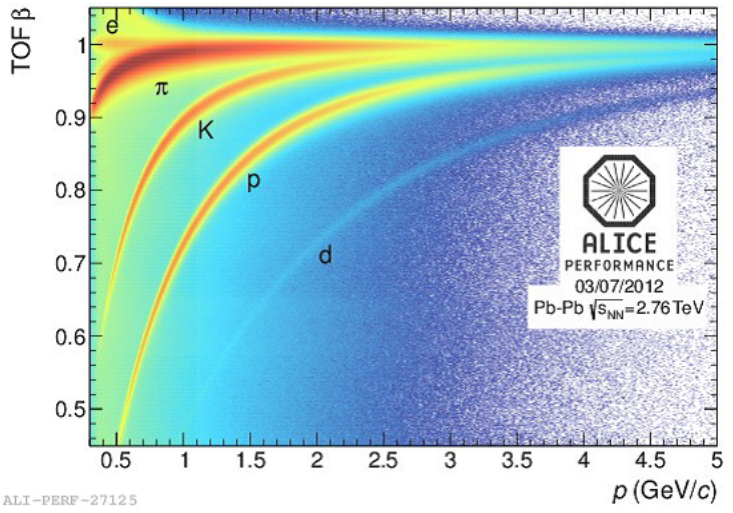

Figure 11: The TOF PID ability

High Momentum Particle Identification Detector (HMPID)

The High-Momentum Particle Identification Detector (HMPID) is dedicated to inclusive measurements of identify hadrons over 1GeV/c. The purpose of HMPID is to enhance the PID capability by enabling identification of charged hadrons beyond the momentum which is not able to be measured by ITS, TPC and TOF. HMPID is based on proximitry-focusing Ring Imaging Cherenkov (RICH) counter.

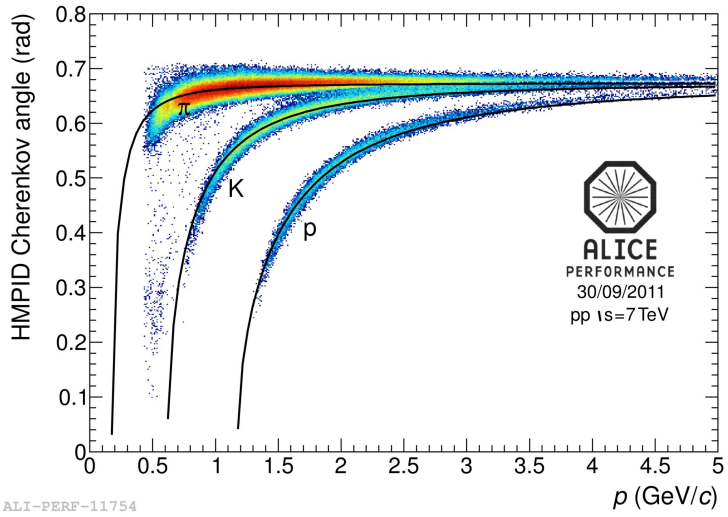

Figure 12: The HMPID PID ability

PHOton Spectrometer (PHOS)

The PHOton Spectrometer (PHOS) is a high-resolution electromagnetic calorimeter covering the rapidity range $|\eta| < 0.125$ and $\Delta\phi = 60°$. The main physics objectives are measurement of direct photon, especially thermal photon, high p_{T} particles decaying into photons and the study of jet quenching. It is installed at point on a distance from interaction point is 460cm and 3 out of 5 modules. One module consists of 64x56 crystals. The crystal is constituted by lead-tungstate (PWO_4) and its size is $22 \times 22 \times 180\mathrm{mm}^3$. The PHOS modules are operated at a temperature of $-25°$C because the PWO's amount of luminescence becomes large.

ElectroMagnetic Calorimeter (EMCal)

The ElectromMagnetic Calorimeter (EMCal) is covering central large region ($|\eta| < 0.7$, $\Delta\phi = 107°$). It is constituted of Pb-scintillator tower and its sige is $60 \times 60 \times 246\text{mm}^3$. It is positioned approximately opposite in azimuth to the PHOS. The EMCal enable us to to explore in the detail of the physics of jet quenching over the large kinematics range accessible in heavy ion collisions.

2.2.2 Muon Spectrometer

The muon specrtometer consists of tracking detector, triggering detector, absorber and dipole magnet . The front absorber is installed inside of solenoid magnet. The fiducial volume of it is mede predominantly out of carbon and concreat to limit small angle scattering and energy loss by transversing muon. Its total length is 4.13m and interaction length is about $10\lambda_{int}$. Five tracking Chambers are installed. two chambers are installed inside of solenoid magnet, one is in dipole magnet and the others are in front of muon filter(Fig.) The filter is made of steal and can reject low momentum muons. The trigger chambers are located beyond the fileter.

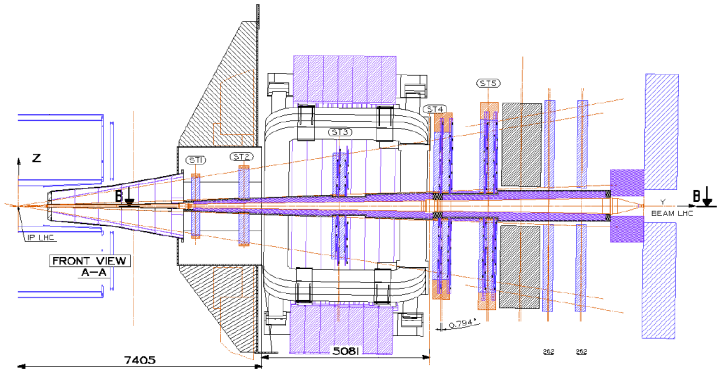

Figure 13: The over view of the Muon spectrometer

2.2.3 Forward Detector

V0 Detector

The information from the V0 detector is from the V0 detector is

used as minimum-bias trigger. It consists of two arrays of scintillator counters that are located in rapidity $2.8 < \eta < 5.1$ (called V0A) and $-3.7 < \eta < -1.7$ (called V0C). The time resolution is about 1 ns wihch can reject beam-gas events that occured outside of the nominal interaction region.

T0 Detector
The T0 detector is able to measure the collision time with a precision of 25 ps. This time information can be used as a reference for the TOF and to determin the primary vertex position with a precision of about 1.5cm. It provides redunduncy to the V0 counters and can generate minimum-baias and multiplicity trigger. The dead time of the V0 and the T0 should be less than the bunch crossing period (25ns).

Forward Multiplicity Detector (FMD)
The main functionarity of the Forward Multiplicity Detector (FMD) consists of silicon stlip detector to measure charged-particle multiplicity in the rapidity range $-3.4 < \eta < -1.7$ and $1.7 < \eta < 5.0$. Combine the FMD and the SPD allows for the study of multiplicity fluctuations on an event by event basis and for the determination of the reaction plane.

Zero Degree Calorimeter (ZDC)
Spectators nucleons are detected by means of Zero-Degree Calorimetes (ZDC). The number of participant nucleons is the observable most directly related to the geometry of A-A collisions. It can be calculated by measuring the energy carried in the forward direction. If all the spectators are detected, the number of participants is given by:

$$E_{ZDC}(\text{TeV}) = 2.76 \times \text{N}_{\text{spectators}} \tag{13}$$

$$N_{participants} = A - N_{spectators} \tag{14}$$

where 2.76 is the collision energy per nucleon of the Pb beam. However, this simple estimation is no longer corect because all spectator nucleons can not be detected. The centrality information provided by ZDC is also used for triggering system. The ZDC being also position-sensitive detector, can give an estimate of the reaction plane in nuclear collisions.

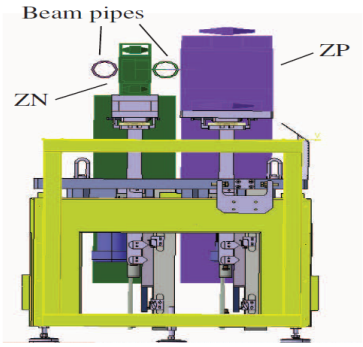

Figure 14: The over view of ZDC

2.3 Trigger and online

2.3.1 Trigger System

The ALICE trigger system is designed to be sufficiently flexible to acquire data during the different run periods and the various types of physics and trigger investigated.

The trigger inputs are divided into three levels,L0, L1, L2 which have different associated latency. The reason why this separation is from properties of the trigger inputs and the detectors. In some detectors require a strobe very early and so a first trigger decision must be delivered within 1.2μs. Owing to the dimensions of detector, this is at the limit of what can be achieved, and a triggering detector will not be able to send its input in time. That is because the fast trigger is divided into two stages.

The whole trigger signals achieve within 1.2μs after collisions are used to make the L0 decision. The other detector signals for trigger which are achieved after that is L1. The third step is L2 trigger which comes after about 88μs The L2 trigger causes the data transfer to the ALICE data acquisition. The L2 reject signal (L2r) can be issued at any time before the fixed latency corresponding to a level-2 accept (L2a) trigger at around 90μs.

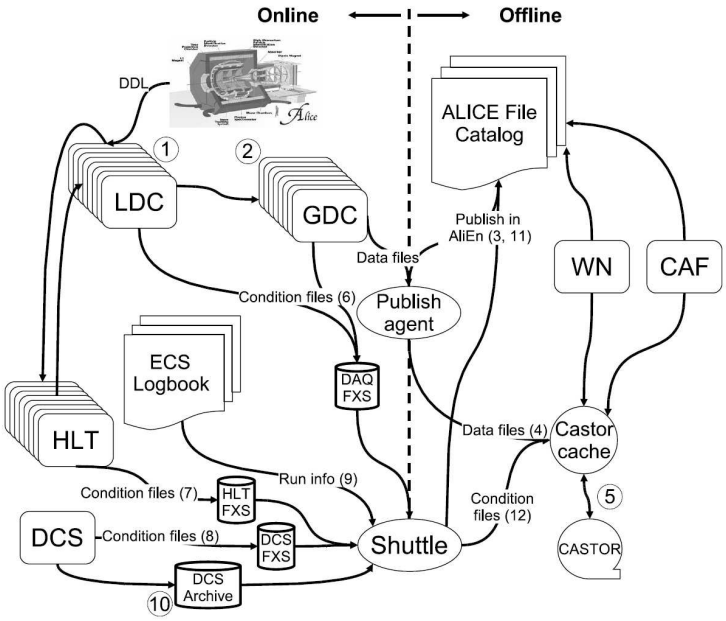

Figure 15: The flow chart of the data from detector

2.3.2 Online computing

The Raw data taken by the subdetectors has to be processed before it is available in the form of reconstructed events for further analysis. This happens in several stages and is illustrated in Fig.15

1. The data taken by detectors is processed by LDCs,
2. The publish agents registers the assembled events into AliEn (ALICE Environment) system.
3. The publish agent ships them to the CERN computing center where they are stored first on disks.
4. And then the data is recorded permanently on tapes by the CASTOR system.

2.4 Offline Computing

AliRoot

The ALICE collaborations has developed the AliRoot, a specific framework for analysis, for example, simulation, alignment, calibration and reconstruction. It is based on the ROOT framework developed by the CERN and is written in C++ and constructed classes for every tasks. The AliRoot has been under development by the ALICE offline project since 1998. The AliRoot also contains reconstruction and analysis code.

Simulation

The flow of the simulation, data taking and reconstruction is shown in Fig.17. The most important thing to note is that the simulations havs the same format as the data stream coming from the DAQ. This gives the most realistic simulations and the best test of the experiment. The ALICE detectors are reconstructed as Fig.16

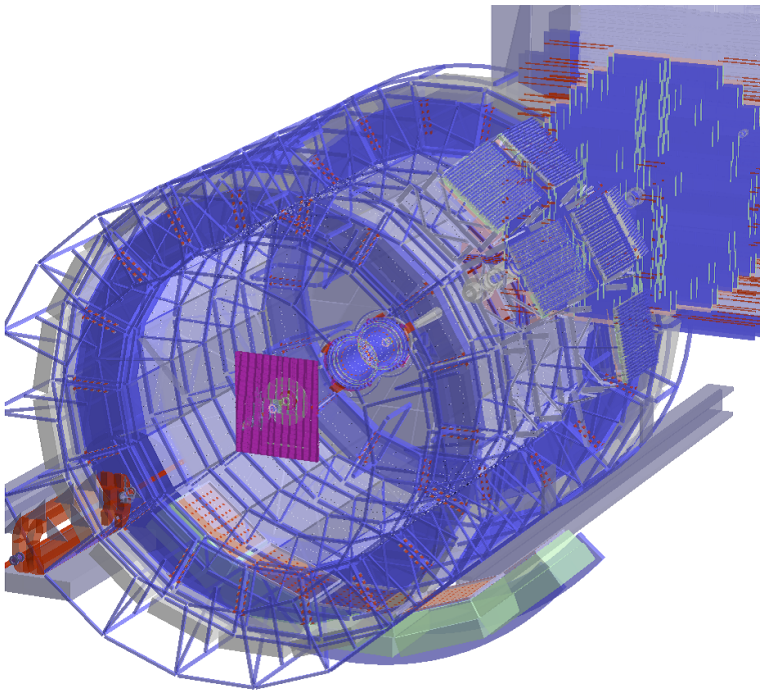

Figure 16: The ALICE detector layout created by GEANT3

The event generator we used in this analysis is so-called Perugia0[17] tuned PYTHIA[16]. It simulates proton-proton collisions. It is based on the QCD calculation and parameters are tuned for pre-

vious experiments results.

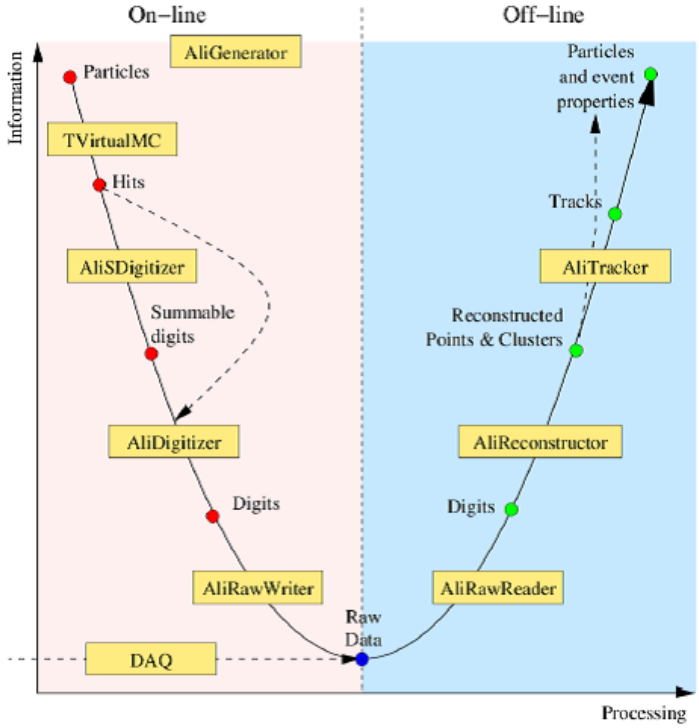

Figure 17: The flow chart of simulation data. The particles generated at left top point., and then reactions of detectors are simulated as real[1].

2.4.1 GRID Computing System

The GRID computing system is resources of computing power and storages in all over the world. It allows users to use them easily. The ALICE produces the huge amount of data ($\sim$ 2PB/year). The world wide distributed GRID facilities were designed to provide both computing power and the disk space. The data taking point namely the ALICE detectors is called Tear-Zero (T-0), the calculating points are Tear-One (T-1) and the storage points are Tear-Two (T-2). The Quark Physics Laboratory of Hiroshima University is a part of T-1.

One of the main advantages in using the GRID is the possibility to analyze a large data set by splitting a job analysis into many

subjobs running in parallel on dierent computing nodes. The ALICE VO (Virtual Organization) is made of more 80 sites distributed in the world (Fig.18).

Figure 18: The map of locations of GRID computers[1].

Each site has many WN on which a programs can run. The SE (Storage Elements) is responsibility for providing an interface to mass storage. The CE (Computing Element) service is an interface to the local batch system and manages the computing resources in the site. AliEn as an implementation of distributed computing infrastructure needed to simulate, reconstruct and analyze data from the experiment. AliEn provides the two key elements needed for largescale distributed data processing: a global le system (catalogue) for data storage and the possibility to execute the jobs in a distributed environment. The analysis software, the user code and the AliRoot libraries needed by each subjob to run must be specied in a JDL (Job Description Language), together with the data sample and the way to split it. The data sample is specied through a XML (eXecutable Machine Language) collection which contains a list of the Logical File Names (LFN, the entries in the catalogue).

3 Performance

3.1 Electromagnetic Calorimeter

Electromagnetic spectrometer can measure photon and electron energy. When the photon goes in the calorimeter, the photon interacts with the matter of calorimeter. High energy photon (MeV $\sim$ GeV) main interaction in a medium is electron and positron pair creation due to the coulomb field created by nuclear and/or orbital electron. High energy electron/positron creates photons due to bremsstrahlung. So, high energy photon creates electrons and positrons and then these electrons and positrons create photons. This interaction continues until the photon energy are lower than the threshold. This phenomenon is called the electromagnetic shower. The higher energy first photon or electron/positron have, the more photons are emitted. We can measure photon or electron/positron energy via the number of photons. A charged particle other than electron/positron can't elicit the electromagnetic shower. These charged particles are called MIP (Minimum Ionizing Particles) and are contamination to measure the photon energy.

3.1.1 PHOS (PHOton Spectrometer)

The PHOS is a high resolution electromagnetic spectrometer covering a limited acceptance domain at central rapidity ($|\eta| < 0.12, 260^\circ < \phi < 320^\circ$). It can measure large dynamic range (0.005-80GeV) photons. The main subjects are measuring thermal and dynamical properties of the initial phase of the collisions, for example, thermal photon and jet quenching through high p_{T} neutral mesons. Measurement in nuclear collisions requires a highly segmented calorimeter with small Moliere radius at a large distance from collision point so that the cell occupancy will be up to $10 - 20\%$. A measurement of mesons requires good position and energy resolution to improve the signal and background ratio for meson identification. Reject Charged hadrons and (anti-)neutron requires high discrimination power for them. TPC, TOF and other tracking detector provide charged particles information to reject charged hadrons. To reject (anti-)neutron, the topological analysis of the shower shape becomes powerful tool. This detector consists of dence scintillator material, lead-tungstate ($PbWO_4$), of $20X_0$ with high photon-electron yield.

3 modules out of 5 are installed and each detector is segmented into 3584 (64×56) cells. The cell consists of $22 \times 22 \times 180\text{mm}^3$ PWO_4 crystal attached a $5 \times 5\text{mm}^2$ Avalanche Photo-Diode (APD). The energy resolution is PHOS is :

$$\frac{\sigma_E}{E[\text{GeV}]} = \sqrt{(\frac{0.0130 \pm 0.0007}{\text{E[GeV]}})^2 + (\frac{0.0130 \pm 0.0007}{\sqrt{E[\text{GeV}]}})^2 + (1.12 \pm 0.3)^2} \quad (15)$$

The high spatial resolution is :

$$\sigma_{x,y}[\text{mm}] = \sqrt{(\frac{3.26}{\sqrt{E[\text{GeV}]}})^2 + 0.44^2} \quad (16)$$

The resolution of two photons invariant mass at the π^0 peak is 3.5%. The timing resolution is about 2ns at energies above 1.5GeV.

To increase the light yield of the PWO crystals, the PHOS modules are operated at a temperature of $-25°$C. To maintain the temperature, all modules are located inside a cold enclosure. All cells have one LED unit and stable current generator to calibrate them.

3.2 Track reconstruction

3.2.1 Traking Detector TPC (Time Projection Chamber)

The main tracking device of the ALICE experiment is a large volume ($\sim 88\text{m}^3$), cylindrical Time Projection Chamber (TPC). The choice of the gas mixture ($\text{Ne} - \text{CO}_2 - \text{N}_2$) implies a non-saturated drift velocity at the nominal drift field (400 V/cm). The consequence is that a temperature stability and homogeneity of $\Delta T < 0.1$ deg is required in order to exhaust the intrinsic detector resolution. The main performance goals considered in the design are a dE/dx resolution better than 5%, a relative p_{T} resolution better than 1% for momenta of about 1 GeV/c and better than 2.5% for momenta of 4 GeV/c, and two track resolution capable for separating tracks with a relative momentum difference of < 5MeV. The expected maximum multiplicity in Pb-Pb collisions at LHC energies was $dN_{ch}/d\eta \sim 8000$ at midrapidity, resulting in about 20000 charged primary and secondary particles in the TPC volume. This number requires the enormous volume for the TPC to obtain the

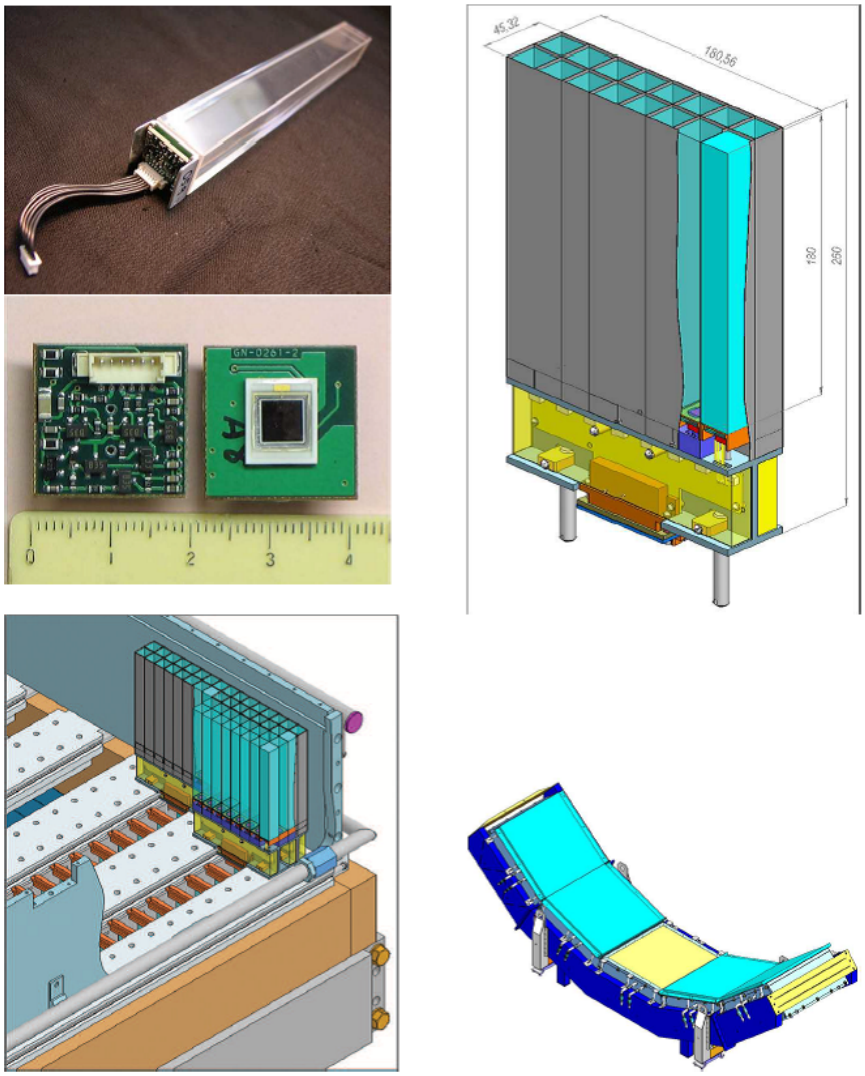

Figure 19: Left top: Crystal detector unit with glued photo-detector; photo-detector, APD mounted on the preamplifier substrate. Right top: Strip unit containing 8×2 crystal detector units. Left bottom: PHOS module with strip units installed onto cooling plates. Right bottom: 5 PHOS modules.

enough track resolution. The TPC is separated into two volumes with the Central Electrode (CE), and electrons generated by projected particles are read by pad-readout chambers located at both sides (A-side for positive-z side and C-side for negative-z side). Each side has 18 Inner Readout Chambers (IROCs) and 18 Outer Readout Chambers (OROCs).

3.2.2 Track Reconstruction Algorithm

The reconstructed TPC tracks and clusters are expressed in the local coordinate system of the y and z of the interaction point of a track and pad row at a given x coordinate are then given by the equations:

$$y(x) = y_0 - \frac{1}{C} - \sqrt{1 - (Cx - \eta)^2}$$
$$z(x) = z_0 - \frac{tan\lambda}{C} arcsin(Cx - \eta)$$
$$\eta \equiv Cx_0$$

where C is the curvature of the track projection on the pad plane, λ is the dip angle between the track and the pad plane, (x_0, y_0) are the coordinates of the center of the curvature of the track projection on the pad plane, and $z_0 \equiv z(x_0)$.

The track state vector X^T used in the Kalman filter calculation is then chose as

$$X^T = (y, z, c, tan\lambda, \eta)$$

With this track parametrization, only two of the five components of the state vector (the local track position y and z) change as the track is propagated from one pad row to the other. These calculations are done 159 times (the number of TPC pad rows) per a track. When a track is leaving one sector and is entering another, the coordinate system is rotated, then three components y, z and η have to be changed.

The Kalman filter propagation begins with the seed finding at the outer side of TPC, where track density is lower than near the primary vertex. Fig.21 shows the relative momentum resolution of the ALICE-TPC measured in cosmic runs before the start of LHC runs.

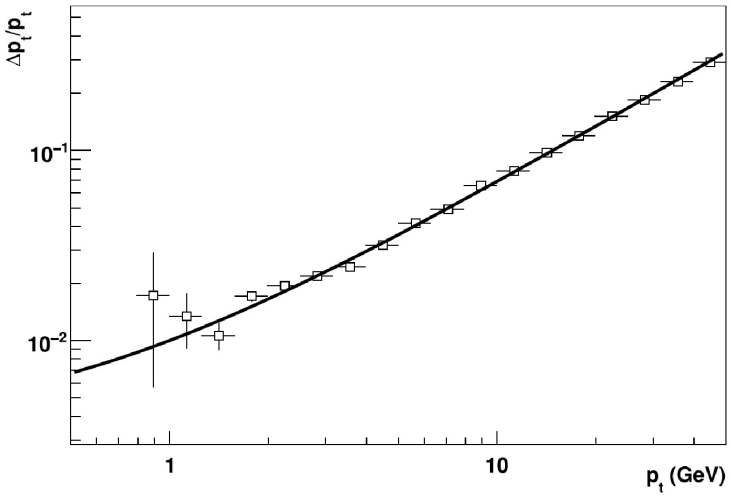

Figure 20: Relative momentum resolution at the ALICE-TPC[6]

3.3 Trigger Criteria

Various triggers can be configured simultaneously and more complex trigger patterns can be implemented in the High Level Trigger (HLT). We used two triggered data in this analysis. One is Minimum bias trigger and the other one is high energy photon trigger called PHOS triggered data. I will introduce these trigger criteria in this section.

ALICE trigger is organized in the following way: Each run contained minimum bias trigger and many rare-event triggers, including the PHOS trigger. All triggers rotated with a 4-minute period: a few seconds were devoted to minimum bias only, then a few seconds for rare event triggers, and then the loop repeated event 4 minutes (240 sec).

3.3.1 Minimum Bias Trigger

Minimum Bias (MB) trigger is designed to trigger on all inelastic interactions occuring in the detector, event when the momentum transfer between the incoming particles is small or when only very few final state particles are produced. In 2010, 2011 and 2012 runs, the MB trigger criterion in each year is:

- 2010 : V0A | SPD | V0C.
- 2011 : V0A & SPD & V0C.
- 2012 : V0A & SPD & V0C.

In 2010, MB trigger is required V0A or V0C or SPD have at least one hit. In 2011 and 2012 runs, all V0A, V0C and SPD second layer have at least one hit.

3.3.2 High p_{T} Photon Trigger (PHOS Trigger)

The PHOS trigger main purpose is measurement of the high energy photon. The TRU (Trigger Region Unit) is the main circuit to judges the events. The TRU consists of a chip called the FPGA (Field Programmable Gate Array). One module has 8 TRUs and one TRU has 14 FEE cards. One FEE cards collects the information from 32 channels as the FAST-OR signal. The FAST-OR signal is a sum of 4 (2x2) channels signal. So, one FEE treats 8 FAST-OR signals and one TRU handles 14 x 8 = 112 FAST-OR signals. Fig.22 shows makeup of the PHOS one module. All TRU (8 TRU x 3 modules = 24TRU) information are collected by the TOR (Trigger OR). The TOR deals with 2x2 signals from the TRU as 1 unit. In fact, the TOR handles 4x4 = 16 channels. The way of sum up is shown in Fig.25. 91 combinations of 2x2 FAST-OR units are created from one TRU region.

If at least one 2x2 FAST-OR unit is over the threshold and V0A and V0C both have at least one hit, those events are PHOS triggered events.

- 2011 : V0A & 0PH0 & V0C (PHOS threshold 2GeV).
- 2012 : V0A & 0PH0 & V0C (PHOS threshold 2GeV and 4GeV).

0PH0 means at least one 2x2 FAST-OR unit reacts.

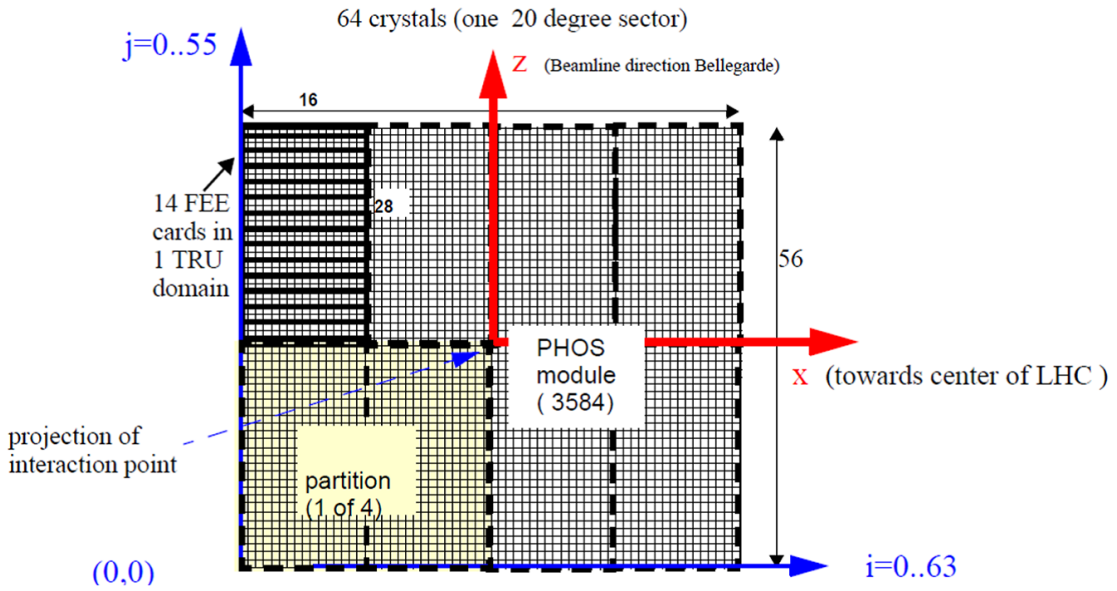

1 FEE	1 RCU branch	1 RCU partition	1 PHOS module
32 input channels 64 readout channels each two 10 bit readout channels HG and LG	14 FEE cards 1 TRU card 448 input channels 896 readout channels	2 branches A+B 2 x 14 FEE cards 2 TRU cards 896 input channels 1792 readout channels	112 FEE cards 8 TRU domains 8 RCU banches 4 RCU partitions 3584 input channels 7168 readout channels 10 bit

Figure 21: Geometry and labels of the PHOS

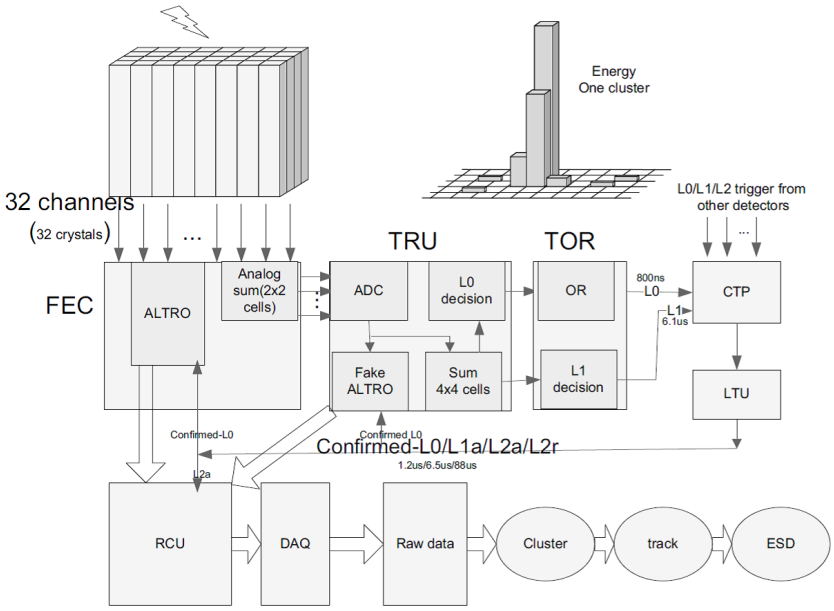

Figure 22: The dataflow of the PHOS trigegr and readout system[12].

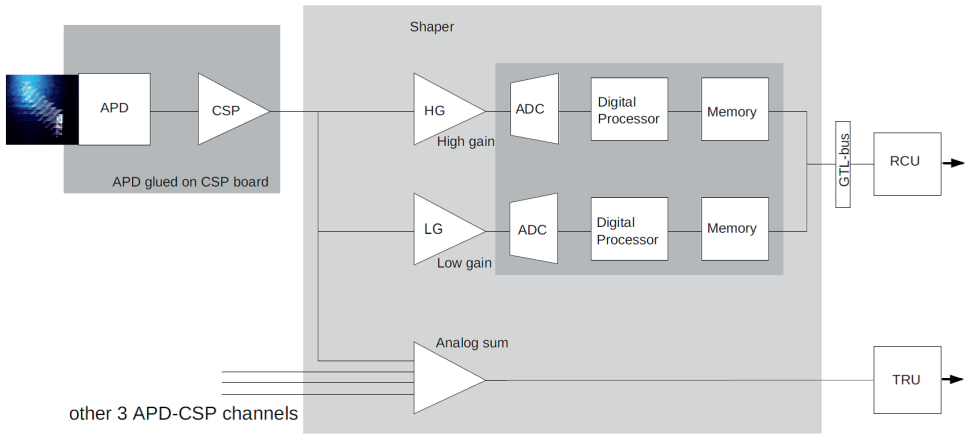

Figure 23: The signal path of POHS. The signal from the CSP output is split into threeparts, two parts (high gain and low gain) are digitized for data analysis, and the other part (Analog-sum) gose into the TRU for trigger processing[12].

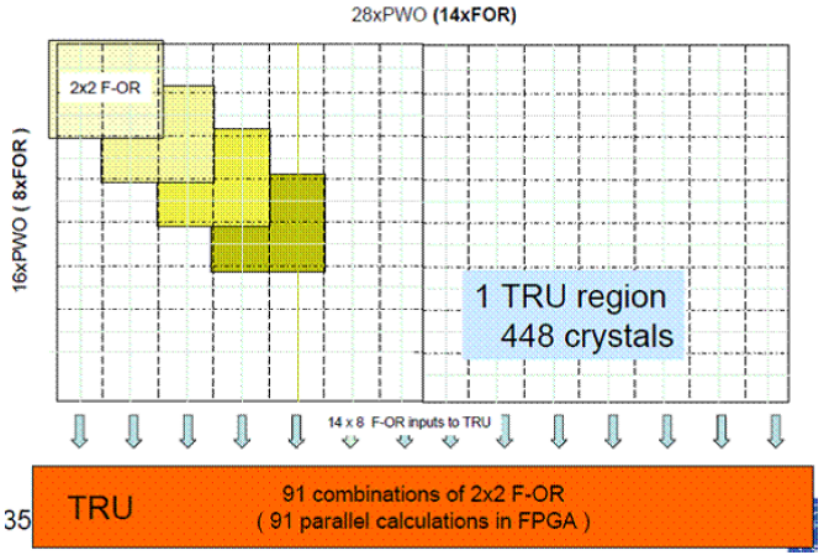

Figure 24: How to combine the Fast OR signals. One TRU has 14×8 the FAST-OR signals, One TRU has $13 \times 7 = 91$ units.

4 Analysis

4.1 Run Condition and Selection

The data of $\sqrt{s} = 8$TeV $p - p$ collisions used in this analysis were taken by ALICE experiment in 2012. It started from 4th April to 15th December. During this period, the ALICE collected about 10pb^{-1} integrated luminosity in 2012(Fig.26). This statistic is about 2times larger than that of 2011. The ALICE divides data taking period into some periods due to various reasons. The data period I analyzed is called LHC12c and it was taken from 1st May to 17th June. The LHC information during this interval is that peak luminosity is $30.28 \times 10^{30}\text{cm}^{-2}\text{s}^{-1}$, beam1 and beam2 intensity are 41.32×10^{12} and 41.36×10^{12}, beam energy per proton is 4000GeV and number of bunches is 396.

I selected runs which are passed several Quality Assurance (QA) and I applied three criteria to select runs. One is the number of PHOS clusters per event. If the PHOS had many noisy channels in a run, the number is larger than other runs. Second is π^0 mass

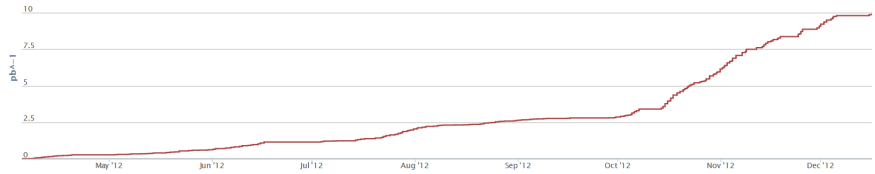

Figure 25: The luminosity taken by the ALICE[8]

peak QA to find miss energy calibration runs. The other one is the number of tracks per event. Fig.27, Fig.28 and Fig.29 show you the number of clusters, π^0 mass peak position and the number of tracks per event respectively. All histograms of three, the horizontal axis is run number index and the vertical axis is each QA values. The number of clusters per event of module 2 has some runs are wrong but other runs and module 1 and module 3 results are stable. The π^0 mass peak position of all modules are very stable. Fig.28 confirms energy calibration of all modules were fine. The Track QA also confirms that tracking systems didn't have something wrong at all runs in this period.

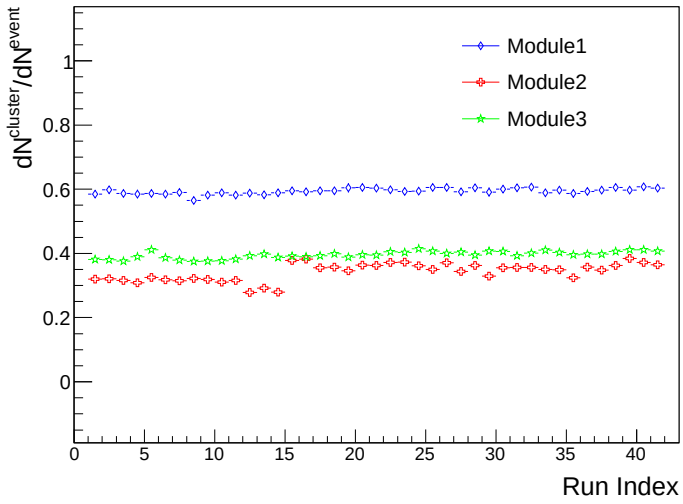

Figure 26: The number of clusters per event vs run number.

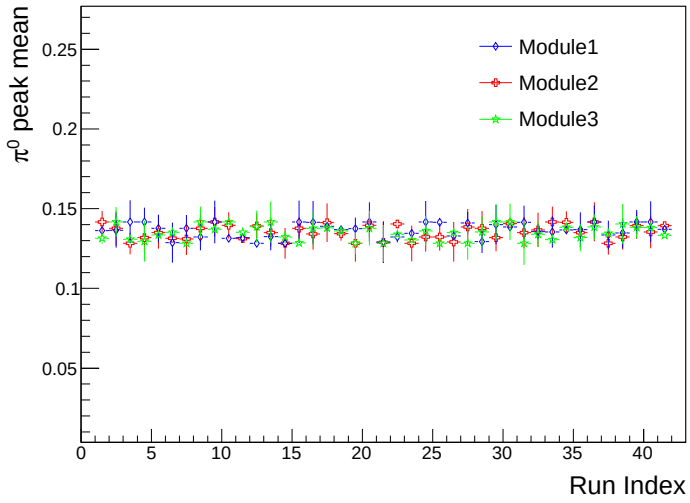

Figure 27: The π^0 peak position vs run number.

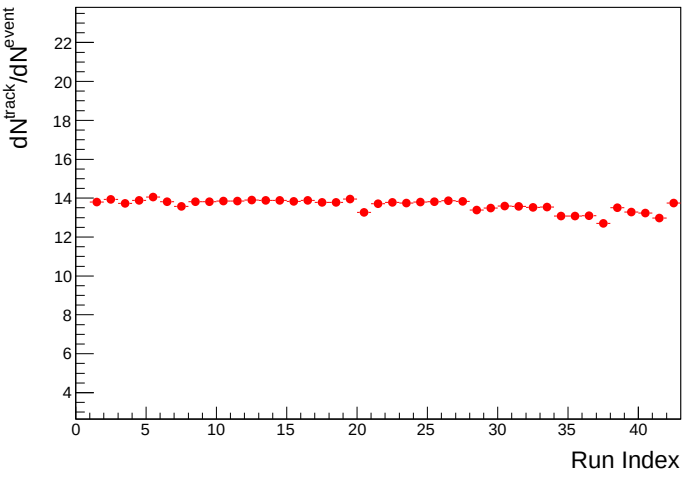

Figure 28: The number of tracks per event vs run number.

4.2 Rejection factor of the PHOS trigger

The ALICE has about 50 trigger classes to observe more physics topics. In this analysis, the PHOS trigger was used to measure higher p_{T} particles than MB. The PHOS trigger is sensitive for detection of high energy photon. It is rare for MB trigger in proton-proton collisions to observe high energy photons. However, the PHOS trigger gathers high energy photon events selectively. The rejection factor indicates how rare the PHOS trigger is. The rejection factor is defined as following in this analysis.

$$R = \frac{L2b_{PHOS}}{L2b_{MB}} \frac{\tau_{MB}}{\tau_{PHOS}} \tag{17}$$

where L_2^{MB} is the number of L2 MB triggered evens and L_2^{PHOS} is that of the PHOS trigger. τ_{MB} and τ_{PHOS} are share time of MB and the PHOS trigger respectively[11]. These L_2^{MB}, L_2^{PHOS}, τ_{MB} and τ_{PHOS} are different from run by run. Therefor the rejection factor is calculated run by run.

The inelastic cross section σ_{inel} of proton-proton collisions at $\sqrt{s} = 8$TeV is measured by the TOTEM experiment[9]. The ALICE MB trigger in 2012 required both VZERO-A and VZERO-C have at least one hit. The relationship of the cross section of MB trigger σ_{MB} to inelastic cross section σ_{inel}has been calculated with Monte Calro simulation[4].

$$\sigma_{inel} = 74.7 \pm 1.7\mathrm{mb} \tag{18}$$

$$\sigma_{MB}/\sigma_{inel} = 0.799 \pm 0.012 \tag{19}$$

$$\sigma_{MB} = 59.7 \pm 1.6\mathrm{mb} \tag{20}$$

and the PHOS trigger cross section is as following.

$$\sigma_{PHOS} = \sigma_{MB} \times R \tag{21}$$

where R is rejection factor of each run.

4.3 Photon Cluster Selection Criteria

The dispersion cut is applied to cluster selection. The dispersion cut constrains the cluster shape to reject clusters created by other than a photon. We decide the cluster is created by whether a photon or

not with equation(22).

$$R^2 = \frac{(l1 - l1Mean)^2}{\sigma_{l1}^2} + \frac{(l2 - l2Mean)^2}{\sigma_{l2}^2} - c \cdot \frac{(l1 - l1Mean)(l2 - l2Mean)}{(\sigma_{l1})(\sigma_{l2})} \quad (22)$$

where $l1$ is M20 (short axis) and $l2$ is M02 (long axis). These M20 and M02 are shown in Fig.30. And the other parameters are as a function of p_T and fixed as below.

$$l1Mean = 1.123 + 0.123 * e^{-p_T * 0.246} + 5.3 * 10^{-3} * p_T$$
$$l2Mean = 1.531 + 9.508 * 10^6 / (1 + 10.087 * 10^7 * p_T + 1.734 * 10^6 * p_T^2)$$
$$\sigma_{l1} = 4.447 * 10^{-4} + 6.998 * 10^{-1} / (1 + 1.225 * p_T + 6.786 * 10^{-7} * p_T^2) + 9.000 * 10^{-3}$$
$$\sigma_{l2} = 6.482 * 10^{-2} + 7.603 * 10^{10} / (1 + 1.530 * 10^{11} * p_T + 5.012 * p_T^2)$$
$$c = -0.35 - 0.550 * e^{-0.391 * p_T}$$

When the R^2 of cluster is $R^2 < 2.5^2$, the cluster is assumed that it is a photon cluster.

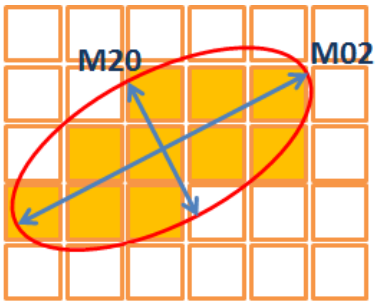

Figure 29: The cluster shape. Definition of M20 and M02 which are used in the dispersion cut.

4.4 Track Selection

In this analysis, all charged tracks are assumed as charged pion because generated particles are almost charged pions. The table shows track quality cut criteria.

Selection	*Value*
Detector requirement for track rec./refit	*ITS, TPC*
Number of TPC cluster	> 70
$\chi^2/N_{cluster}$ *in TPC*	< 4
Cluster in ITS	*Not require*
DCA_{xy}	$< 0.5cm$
DCA_z	$< 2cm$

This set of cuts is very close to the multiplicity analysis. However, in this analysis, we apply loose the DCA cut and don't require SPD hit for tracks. We observed that when we required at least one SPD hit in the charged track we significantly decrease reconstruction efficiency for ω. It happens because of the SPD dead regions which are located close to the PHOS acceptance in azimuth. Another important things is that tracks with and without the SPD hits have quite different DCA resolution. That is reason why we apply these cut in this analysis.

The charged pion from the ω which decays into 3 pion and π^0 going to the PHOS goes almost to the PHOS acceptance. So, in this analysis, we select $|\eta| < 0.4$ and $235^\circ < \phi < 335^\circ$ tracks.

4.5 Reconstruction of π^0 and η from 2 photons

This section explaines how to reconstructed π^0 and η meson from 2γ. 2γ are observed by PHOS.
Invariant Mass is calcurated with function below.

$$M_{12} = \sqrt{E_1^2 + E_2^2 - (\vec{p}_1 + \vec{p}_2)^2} = \sqrt{m_1^2 + m_2^2 + 2(E_1 E_2 - \vec{p}_1 \cdot \vec{p}_2)} \quad (23)$$

where $\vec{p}_1, \vec{p}_2$ and m_1, m_2 are momentum and mass of particle 1 and particle 2. Photon mass is $m = 0[\mathrm{GeV/c^2}]$ and above equation can be determined as following.

$$M_{\pi^0} = \sqrt{2E_1E_2(1 - cos\theta_{12})} \quad (24)$$

θ_{12} is opening angle of two photons from the mother particle.

We apply cluster energy asymmetry cut to two clusters combination for π^0 and η reconstruction. The energy asymmetry is defined

as:

$$\alpha = \frac{|E_{\gamma 1} - E_{\gamma 2}|}{E_{\gamma 1} + E_{\gamma 2}} = |\beta cos\theta|$$

where $E_{\gamma 1}$ and $E_{\gamma 2}$ are $\gamma 1$ and $\gamma 2$ energy. We apply $\alpha < 0.8$ cut to get more signal significance.

The invariant mass distribution of $4 < p_{\mathrm{T}} < 6$GeV/c of each particles are shown in Fig.31.

4.6 Reconstruction of ω and η from π^0 and $\pi^{\pm}$

The ω is reconstructed from π^0, π^+ and π^-. First of all, we select the π^0 from 2γ with the PHOS. Invariant mass of the ω is calculated with equation(23). Then we measure π^+ and π^- with the ALICE tracking system and calculate the invariant mass of these three particles with following equation.

$$M_{\pi^0\pi^+\pi^-} = \sqrt{E^2_{\pi^0} + E^2_{\pi^+} + E^2_{\pi^-} - (\vec{p}_{\pi^0} + \vec{p}_{\pi^+} + \vec{p}_{\pi^-})^2} \qquad (25)$$

The π^0 candidates are selected from invariant mass around π^0 mass region in invariant mass distributions of 2γ.

4.7 PHOS Bad channels Map

Some channels of the PHOS doesn't work well. The information from these channels are not correct. The bad channel is separated into three classes. The two criteria are used for this analysis.

1. Number of cell was the leading one in a low energy cluster
2. Number of cell was the leading one in a high energy cluster

Where "low energy" corresponds to clusters with energy $0.3 < E < 1.0$GeV, while "high energy" corresponds to clusters with energy $E > 1.0$GeV. Now, for each of the two criteria, for each run and for each cells we calculate the cell factor.

$$\text{factor} = \text{cell value/average over cells} \qquad (26)$$

The factors for criteria 1 and 2 results are shown in Fig.32.

- factor ~ 1 : the cell has the same behaviour than average

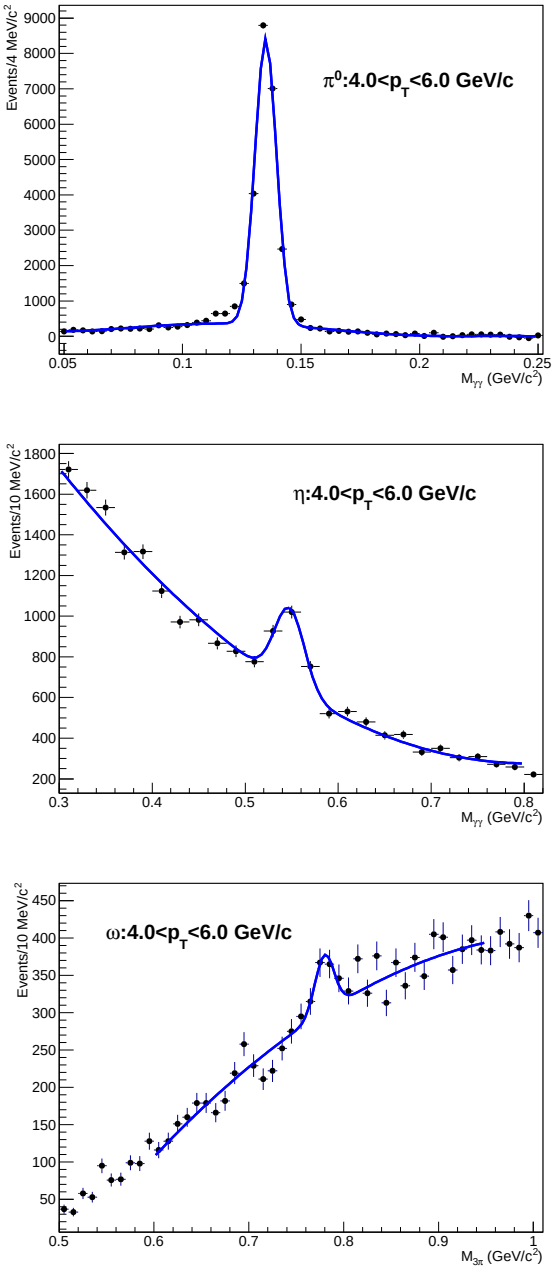

Figure 30: Top: π^0 mass peak from 2γ. Middle: η mass peak from 2γ. Bottom: ω mass peak from 3π.

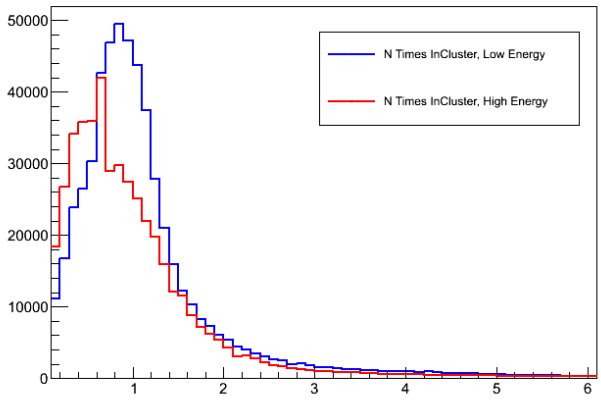

Figure 31: Factor distribution

- factor $\ll 1$: the cell contributes less to clusters than average
- factor $\gg 1$: the cell contributes more to clusters than average

We decide noisy channels and dead channels following definition.

- Dead cell candidate : factor ≤ 0.05 for criteria 1
- noisy cell candidate : factor ≤ 3.5 for criteria 1 or 2

From these criteria, the bad channels are estimated as Fig.33. In Fig.33, the light green points are the dead channels and the red points are the noisy channels.

4.8 Acceptance x Reconstruction efficiency

In this analysis, reconstruction efficiency doesn't include trigger efficiency. This normalizes the raw yield to 2π in azimuth and ± 0.5 units in rapidity for the minimum bias. We estimated it using the simulation. The acceptance x reconstruction efficiency is written as following.

$$= \frac{Acceptance \times Reconstruction\ efficiency}{\begin{array}{c} Rreconstructed\ by\ detector \\ \hline Generated\ by\ simulation\ (\Delta\theta = 360, |\eta| < 0.5) \end{array}} \tag{27}$$

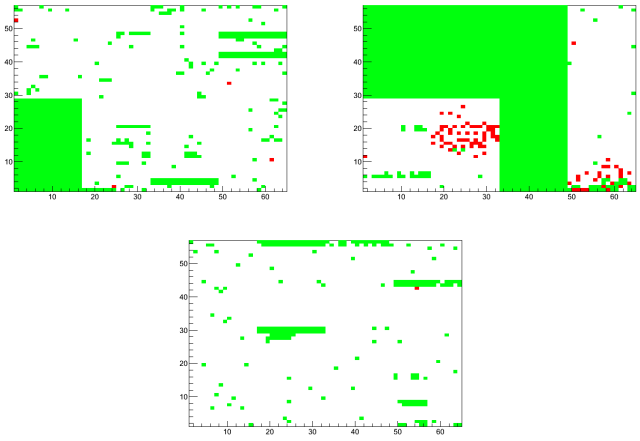

Figure 32: Green regions are dead channels and red are noisy channels. Left: module1. Right: module2. Bottom: module3.

The PHOS covers about 4% of a unit rapidity and about 70% cells are working. The photon purity gets better but efficiency comes down when we applied the dispersion cut for clusters. The photon efficiency for the dispersion cut is about 50% for high pT photons. From these aspects, the efficiency should be about 1.4% at high p_{T}[14].

4.9 PHOS Trigger Efficiency

The trigger efficiency is the probability of firing the trigger. This trigger efficiency is estimated with comparison between the MB and the PHOS trigger cluster distribution. So, in this analysis, the trigger efficiency is used as ratio of PHOS triggered spectrum to MB spectrum. We need the sufficient statistics to estimate the trigger efficiency for π^0, η and ω. However, in this analysis, we estimated them with simulation. This section will explain how to estimate the trigger efficiency.

4.9.1 The Trigger Efficiency for Single Photon

The PHOS triggered events in MB events are found with the TOR signals. We explained the PHOS trigger criteria in section 3.3. First, we accumulated energy spectra for all clusters in all MB events

($MBSP$), and then accumulated energy spectra for cluster fired the trigger ($PHSP$). The ratio of $PHSP/MBSP$ gives the trigger efficiency for one cluster. $MBSP$ and $PHSP$ are shown in Fig.34. The ratio of $PHSP$ to $MBSP$ foe each modules are shown in Fig.36. In Fig.36, the horizontal axis is a cluster energy and the vertical axis is a efficiency. These plots in Fig.36 are all TRU results. Each TRUs results are shown in Fig.35.

In Fig.36, the efficiency of all modules don't achieve 1 because all TRU were not working well. Fig.36 are filled cell positions which fired trigger. As you can see there are many blank trigger regions other than dead cells (see Fig.33, 37 and 38). The CSP signal from APD is split into trigger process and read-out process(Fig.24). There are some cells which are connected to RCU but TRU. In Fig.38, there are regions which are easy to fire the trigger relatively (red spots in 38). Meanwhile, there are also some cells which are not much. to fire the trigger. This is because the efficiency doesn't achieve 1 at high p_{T}.

4.9.2 The TRU response in simulation

The statistic of real data is required to estimate π^0, η and ω trigger efficiency. However, we haven't had such statistic of real data. Therefore, we estimated them with simulation. Now, the PHOS trigger can't be created in simulation. So, we have to re-create the PHOS trigger events in a MB simulation. The plots in Fig.36 indicate that a probability of firing trigger as a function of cluster energy. We calculated a cluster whether firing trigger or not with random numbers in the simulation. For example, a cluster has 3GeV energy in module 2, this cluster firing trigger probability is about 70%, see the plot of middle in Fig.36. In this instance, the random numbers are generated within 0 to 1 and if it is under 0.7, this cluster fires the trigger. Up to 4GeV/c, the plots are used as the probability and over 4GeV/c we used fit result.

The plots in Fig.39 shows you comparison of TRUs each of modules. Black points and red points indicate simulation and real respectively and they are consistent with all TRUs each of modules. The ratio of MB and PHOS trigger cluster energy distribution of each modules are shown in Fig.41. The trigegr efficiency of all TRUs of each modules are shown in Fig.40. The black and red points are same as Fig.39. These simulation data are good agreement with

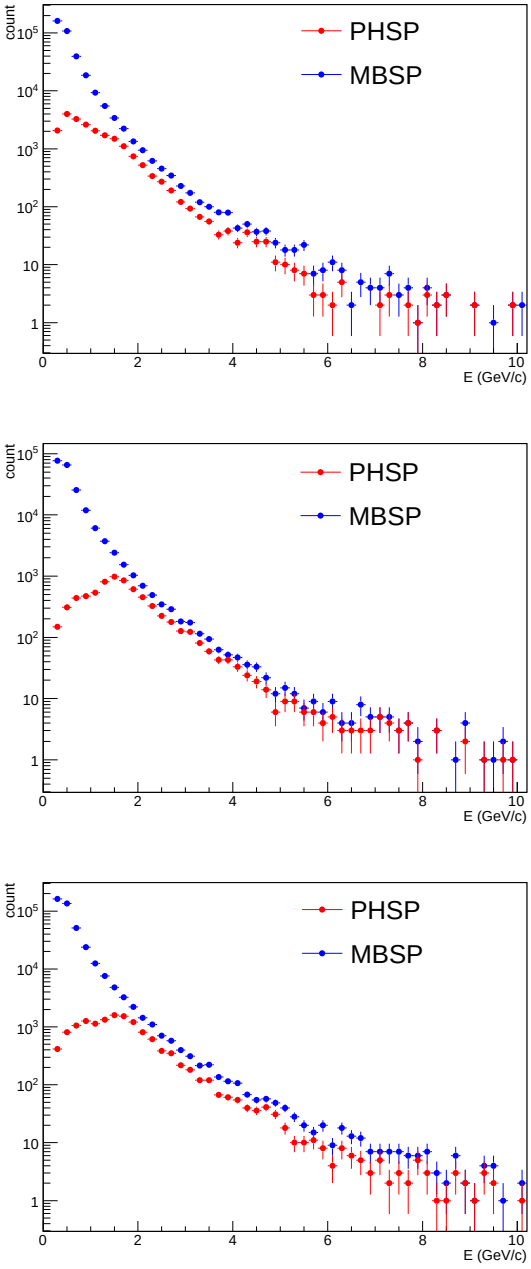

Figure 33: The cluster energy spectra of MB (blue) and firing trigger cluster energy spectra (red). Left: module1. Right: module2. Bottom: module3.

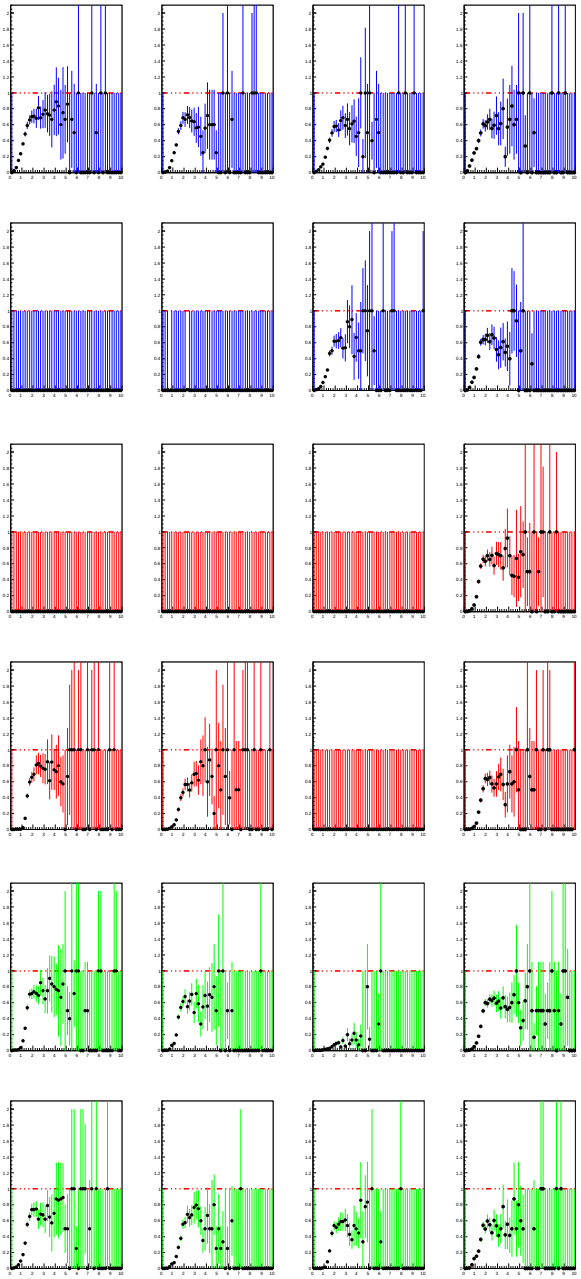

Figure 34: The trigger efficiency of each TRUs. Blue plots are Module1. Red plots are module2. Green plots are module3.

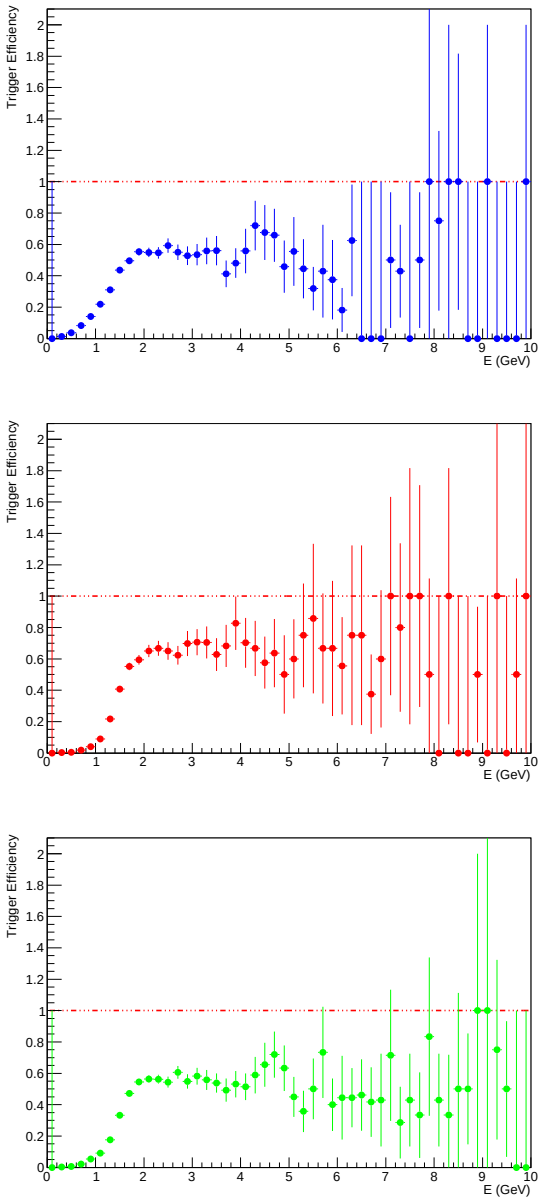

Figure 35: The trigger efficiency of each modules for cluster. Top: module1. Middle: module2. Bottom: module3.

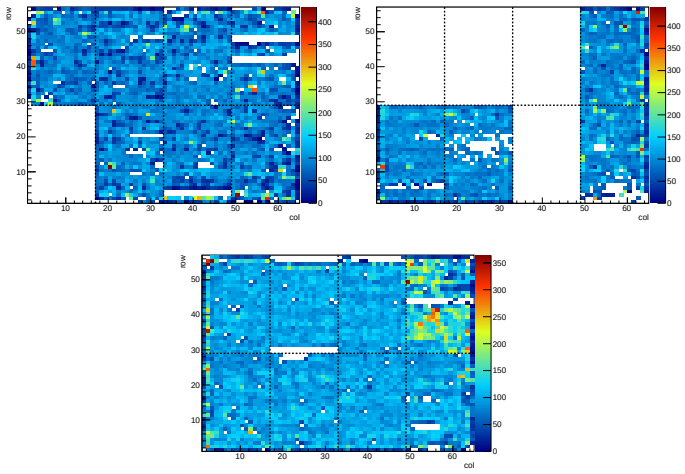

Figure 36: All cluster occupancy of each modules. Left: module1. Right: module2. Bottom: module3.

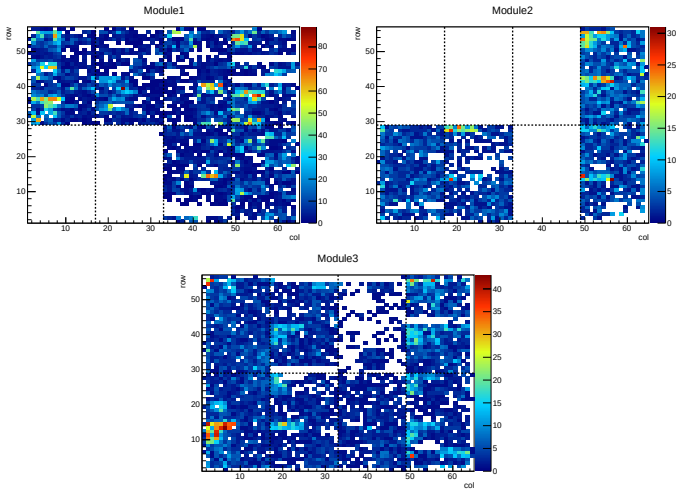

Figure 37: The cluster position firing the trigger maps of each modules. Left: module1. Right: module2. Bottom: module3.

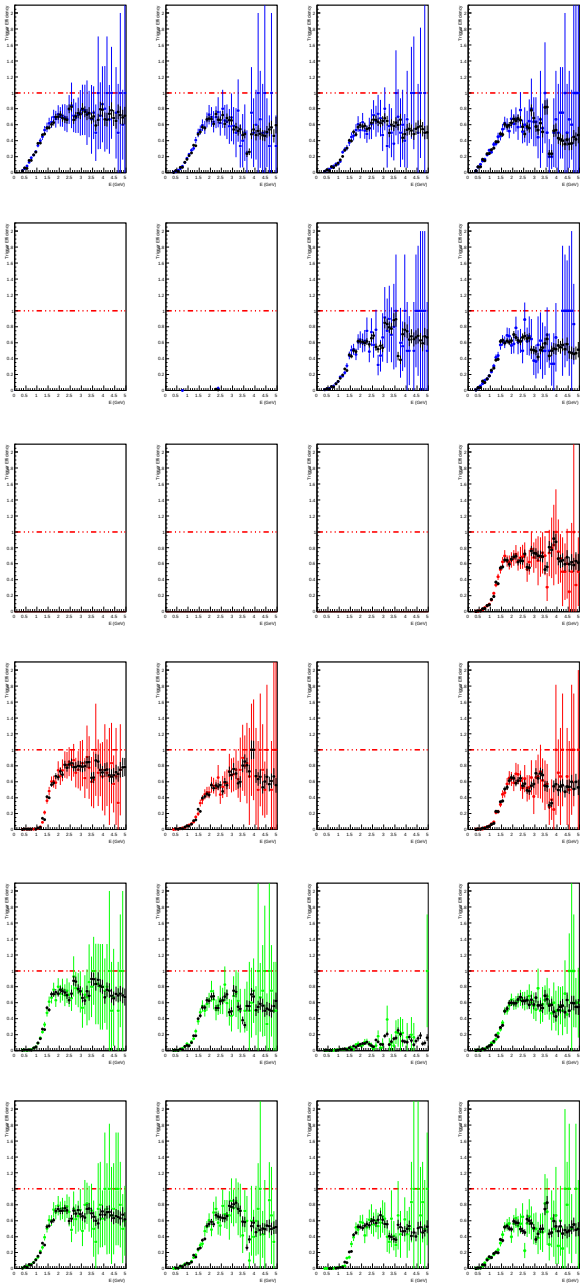

Figure 38: The simulated TRU response for clusters. Color plots and black plots are real and simulation respectively.

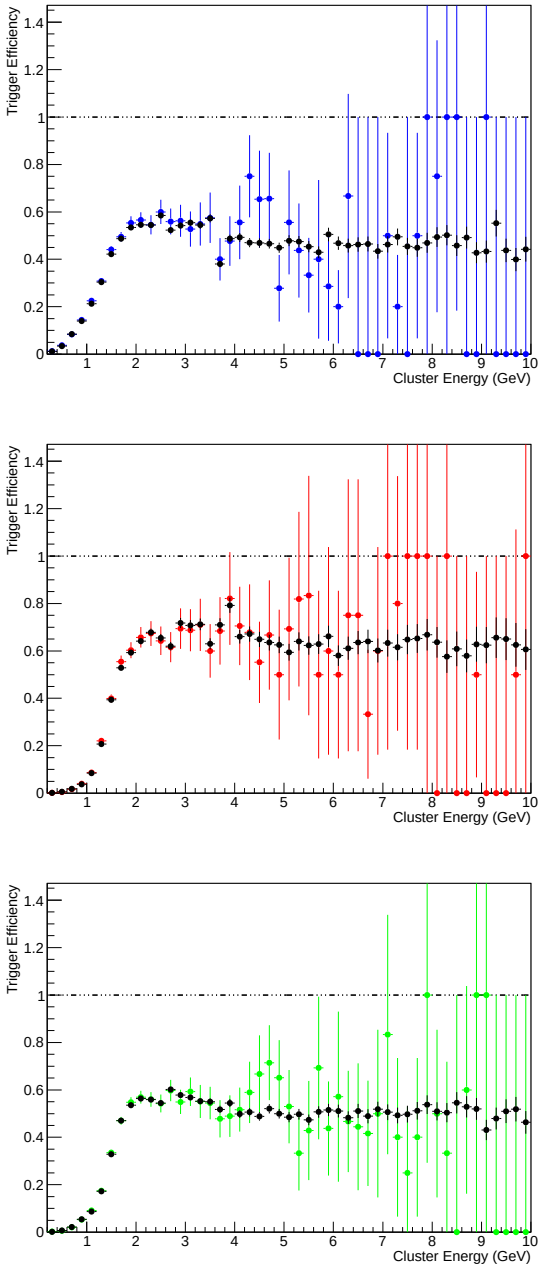

Figure 39: The simulated trigger response for clusters of each modules. Top:module1. Middle:module2. Bottom:module3.

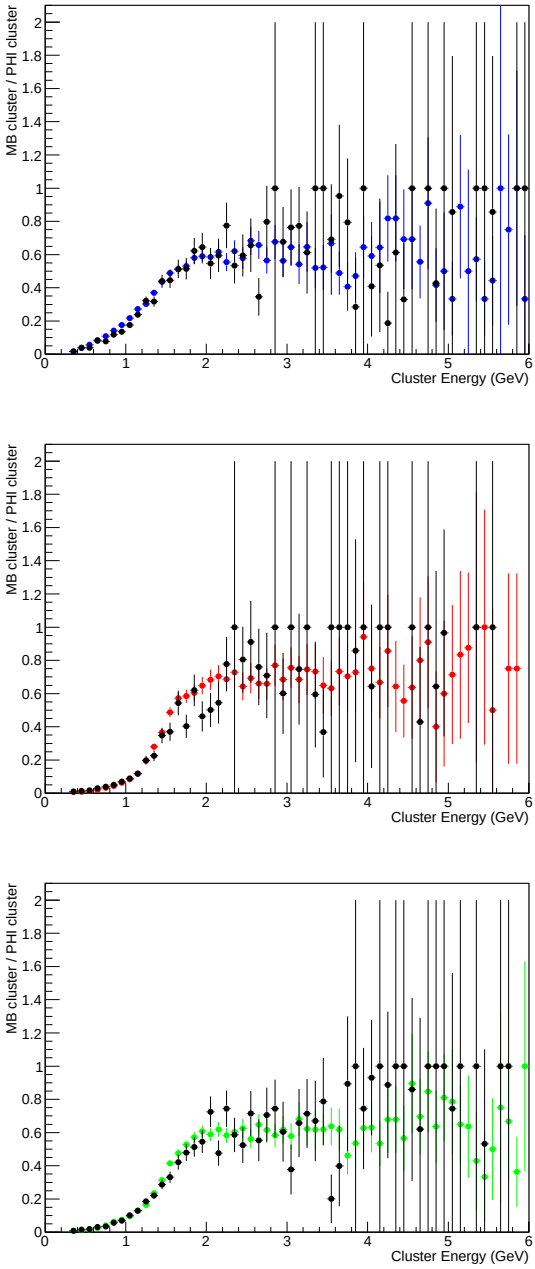

Figure 40: The cluster energy distribution ratio of MB to PHOS trigger in real and simulation. Color plots are real and black plots are simulation data.

real data and we become successful to recreate the PHOS triggered events in simulation.

4.9.3 π^0, η and ω trigger efficiency

The trigger efficiency of π^0, η and ω are estimated by simulation. The TRU response is simulated very well as previous section. The trigger efficiency is defined as following.

$$\epsilon_{trig}^{\pi^0/\eta/\omega} = \frac{The\ number\ of\ reconstructed\ and\ fired\ trigger\ particles}{The\ number\ of\ reconstructed\ particles} \tag{28}$$

The result of π^0, η and ω are shown in Fig.42.

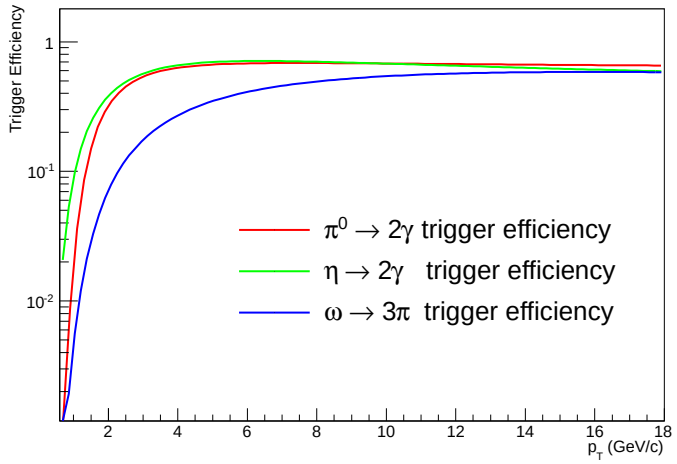

Figure 41: The trigger efficiency of 3 mesons. Red line is $\pi^0 \rightarrow 2\gamma$, Green line is $\eta \rightarrow 2\gamma$, Blue line is $\omega \rightarrow 3\pi$

In Fig.42, a red line is $\pi^0 \rightarrow 2\gamma$, a green one is $\eta \rightarrow 2\gamma$ and blue one is $\omega \rightarrow 3\pi$ results. All efficiencies don't achieve 1 because the efficiency for one cluster doesn't achieve 1. π^0 and η decay into 2 photons and essentially one photon has one second energy of π^0 and η. ω decays into $\pi^0\pi^+\pi^-$. π^0 and $\pi^\pm$ mass are almost same, so π^0 drains about one third energy of ω, and then the π^0 decays 2 photons. One photon energy is about one sixth energy of ω. The threshold plateau point of each modules are about 2GeV (Fig.40).

From these aspects, π^0 and η should have plateau point at around 4GeV/c and ω has it around 12GeV/c. The results of 3 particles in Fig.42 are like that.

There is gap between π^0 and η result. The mass of η is about 550MeV/c^2 and π^0 is about 135MeV/c^2 and these particles go to 2 photons. Therefore there is difference in mass by 400MeV/c^2 and 200MeV/c^2 per one photon. So, one photon from η can have about 200MeV larger than from π^0. A gap between π^0 and η plateau point is about 200MeV in Fig.42.

4.10 Invariant Cross section

The Invariant cross section for π^0, η and ω in proton-proton collisions are calculated as following.

$$E\frac{d^3\sigma}{dp^3} = \frac{1}{2\pi p_{\mathrm{T}}}\frac{1}{\int Ldt}\frac{1}{\epsilon_{trig}\epsilon_{Acc\times Rec}Br}\frac{N}{\Delta y \Delta p_{\mathrm{T}}} \tag{29}$$

where N^{MB}_{event} is scaled the number of PHOS triggered events corresponding to MB events, σ_{MB} is proton-proton collision cross section of MB (both VZERO A-side and C-side have at least one hit) and relative factor $\sigma_{MB}/\sigma^{pp}_{inelastic} = 0.916 \pm 0.013$ estimated from Monte Calro simulation. The inelastic cross section $\sigma_{inelastic}$ of $\sqrt{s}$ = 8TeV proton-proton collisions is measured by the TOTEM experiment group[9]. The ϵ_{trig} and $\epsilon_{Acc\times Rec}$ are the trigger efficiency and acceptance x reconstruction efficiency, Br is the branching ratio, $N/\Delta y \Delta p_{\mathrm{T}}$ is raw yield. The invariant cross section is given from this equation.

4.11 Bin Shift Correction

The deviation of the data points from the true spectrum should be corrected by moving the points along the vertical axis due to the finite bin size. The method of bin shift correction along the vertical axis is as following. First of all, fit the p_{T} spectrum with the following Tsallis function[5],

$$E\frac{d^3\sigma}{dp^3} = \frac{\sigma_{pp}}{2\pi}A\frac{(n-1)(n-2)}{nC[nC+m(n-2)]}(1+\frac{m_T-m}{nC})^{-n}$$

where fit parameters A, C and n, σ_{pp} is the proton-proton inelastic cross section, m is the meson rest mass and $m_T = \sqrt{m^2+p^2_{\mathrm{T}}}$ is the

transverse mass. The property of the Tsallis function is such that the parameter A is equal to production in a unit rapidity dN/dy, T has energy dimension and relevance to the thermal freeze out temperature, and n implies a fluctuation of temperature.

Next, calculate following yield variable m,

$$m = \frac{1}{p_{\mathrm{T}}^{max} - p_{\mathrm{T}}^{min}} \int_{p_{\mathrm{T}}^{min}}^{p_{\mathrm{T}}^{max}} f(p_{\mathrm{T}}^{center}) dp_{\mathrm{T}} \tag{30}$$

and then the correction factor r and the corrected yield can be obtain as,

$$r = m/f(p_{\mathrm{T}}^{center}) \tag{31}$$

$$\frac{dN}{dp_{\mathrm{T}}}|_{corrected} = \frac{1}{r}\frac{dN}{dp_{\mathrm{T}}}|_{corrected} \tag{32}$$

and the process are repeated (iteration).

4.12 Systematic Uncertainties

4.12.1 Detector Uncertainties

The detectors have some uncertainties, energy resolution, energy scale, reconstruction and non-linearity and acceptance uncertainties. The results of that are shown in table[4].

p_{T}, GeV/c	0.6-1.0	1.0-5.0	5.0-10	10-15
Energy resolution (%)	10.5	6	1	1.5
Energy scale (%)	0.5	0.5	0.5	0.5
Reconstruction and non-linearity (%)	6.5	5.0	2.0	1.4
Acceptance (%)	2.0	2.0	2.0	2.0
Tracking efficiency (%)	15	15	15	15

4.12.2 Trigger Efficiency Uncertainties

The main uncertainty of this analysis is from the trigger efficiency. The Monte Calro simulation is used to estimate the efficiency and simulate TRUs response.. However, there is somewhat different points between simulation and real. For example, the cluster energy distribution of cluster energy.

p_T, GeV/c	0.6-1.0	1.0-5.0	5.0-10	10-15
Trigger efficiency (%)	10	20	3	4

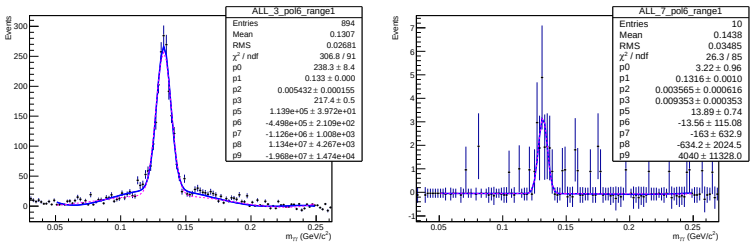

Figure 42: Fits used to estimate systematic uncertainty for π^0 in $4 < p_T < 6$ (Right) and $12 < p_T < 14$ (Left). Gaussian + pol6 (Blue), Gaussian + pol4 (Magenta).

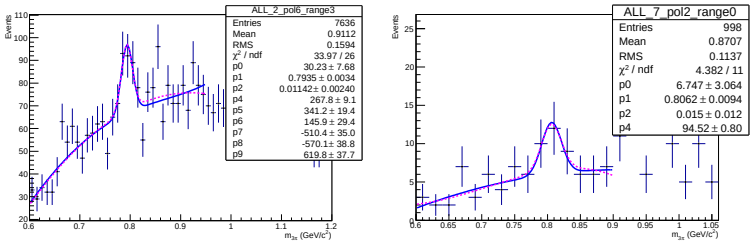

Figure 43: Fits used to estimate systematic uncertainty for ω in $2 < p_T < 4$ (Right) and $8 < p_T < 10$ (Left). Gaussian + pol6 (Blue), Gaussian + pol4 (Magenta).

4.12.3 Peak Extraction Uncertainties

This is the uncertainty for method of signal extraction for the window to count the signal, fitting range and background shape. To evaluate this uncertainty, we use three different fitting functions: the gaussian the first (pol1), the second (pol2) and the third polynomial (pol3). The results are shown in table.

p_T, GeV/c	0.6-1.0	1.0-5.0	5.0-10	10-15
π^0 (%)	x	3	1.5	3.5
η (%)	x	3	2	2
ω (%)	x	3	2	x

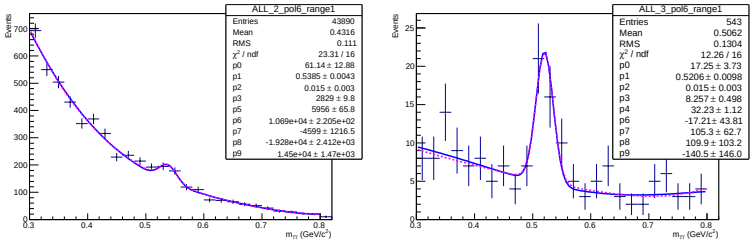

Figure 44: Fits used to estimate systematic uncertainty for η in $4 < p_{\mathrm{T}} < 6$ (Right) and $8 < p_{\mathrm{T}} < 12$ (Left). Gaussian + pol6 (Blue), Gaussian + pol4 (Magenta).

4.12.4 The Other Uncertainties

The other uncertainties are conversion and Off-vertex π^0 uncertainties. Off-vertex π^0 is generated via interaction of charged particles and detector material. These results are in table[4].

p_{T}, GeV/c	0.6-1.0	1.0-5.0	5.0-10	10-15
Conversion (%)	3.1	3.1	3.1	3.1
Off-vertex π^0 (%)	0.12	0.11	0.05	0.04

5 Results and Discussions

5.1 Invariant Cross Section

The invariant cross section of each particles are shown in Fig.46 to Fig.48. The Tsallis function is used to fit spectra and fit parameter results are shown in table below.

The Tsallis function[5] is used to fit spectra.

$$E\frac{d^3\sigma}{dp^3} = \frac{\sigma_{pp}}{2\pi}A\frac{(n-1)(n-2)}{nC[nC+m(n-2)]}(1+\frac{m_T-m}{nC})^{-n}$$

where fit parameters A, C and n, σ_{pp} is the proton-proton inelastic cross section, m is the meson rest mass and $m_T = \sqrt{m^2+p_{\mathrm{T}}^2}$ is the transverse mass. The property of the Tsallis function is such that the parameter A is equal to production in a unit rapidity dN/dy, T has energy dimension and relevance to the thermal freeze out temperature, and n implies a fluctuation of temperature. The fit results are shown in table below.

Mesons	$\sqrt{s}$ TeV	A	C (MeV)	n	Ref
π^0	8	3.05 ± 4.18	138 ± 79	6.3 ± 0.8	This analysis
π^0	7	2.45 ± 0.07	140 ± 4	6.90 ± 0.07	PLB 717 [4]
π^0	0.9	1.5 ± 0.03	132 ± 15	7.8 ± 0.5	PLB 717 [4]

Mesons	$\sqrt{s}$ TeV	A	C (MeV)	n	Ref
η	8	91 ± 640	35 ± 73	5.5 ± 1.5	This analysis
η	7	0.22 ± 0.03	229 ± 21	6.9 ± 0.5	PLB 717 [4]

Mesons	$\sqrt{s}$ TeV	A	C (MeV)	n	Ref
ω	8	88.5 ± 473	13.7 ± 18.7	4.1 ± 0.8	This analysis
ω	7	0.08 ± 0.06	316 ± 122	6.62 ± 1.02	ALICE Preliminary [13]

In this instance, results of low p_{T} region have very large uncertainties because the PHOS trigger is developed to measure high p_{T} particles. Therefore, at low p_{T} region, these spectra are not fitted well. The parameter A and C of the Tsallis function is contributed to a low p_{T} region shape. So, the result of parameter A and C at 8 TeV is regarded as unreliable. The cross sections of η and ω are not fitted well due to limited number of measured points and large uncertainties.

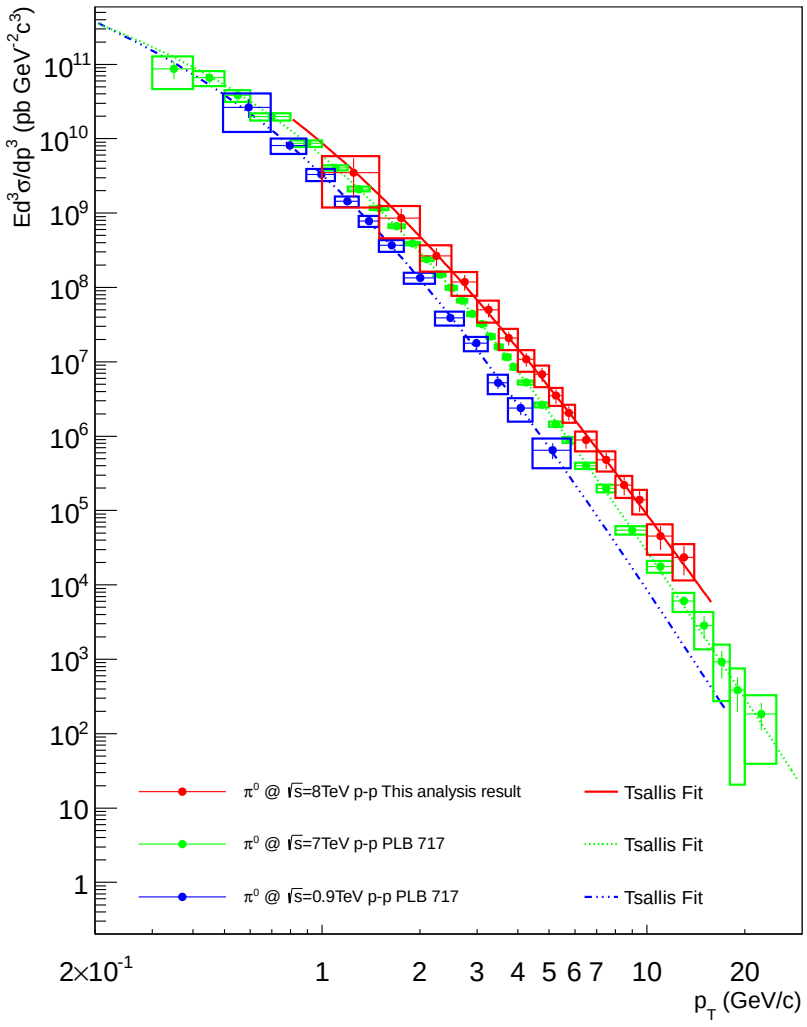

Figure 45: The $\pi^0 \to 2\gamma$ cross sections of different collisions energies. Red: 8 TeV. Green: 7 TeV. Blue: 900 GeV. 7 TeV and 0.9 TeV results are in [4]

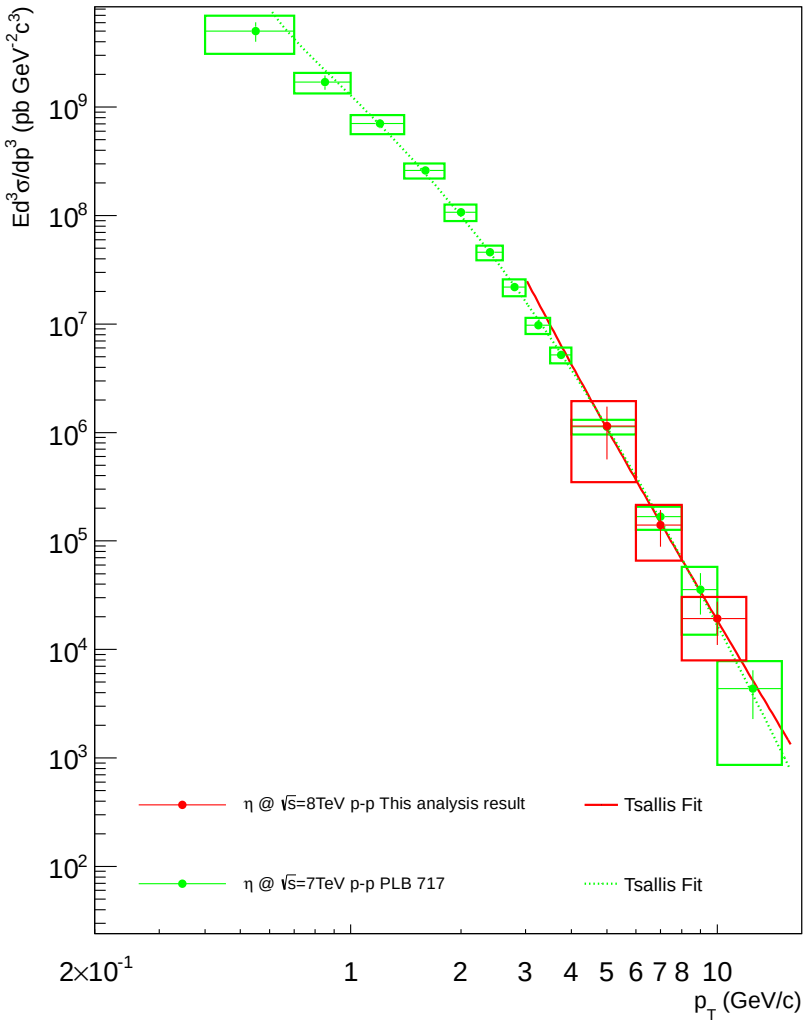

Figure 46: The $\eta \to 2\gamma$ cross sections of different collisions energies. Red: 8TeV. Green: 7TeV. 7 TeV result is in [4]

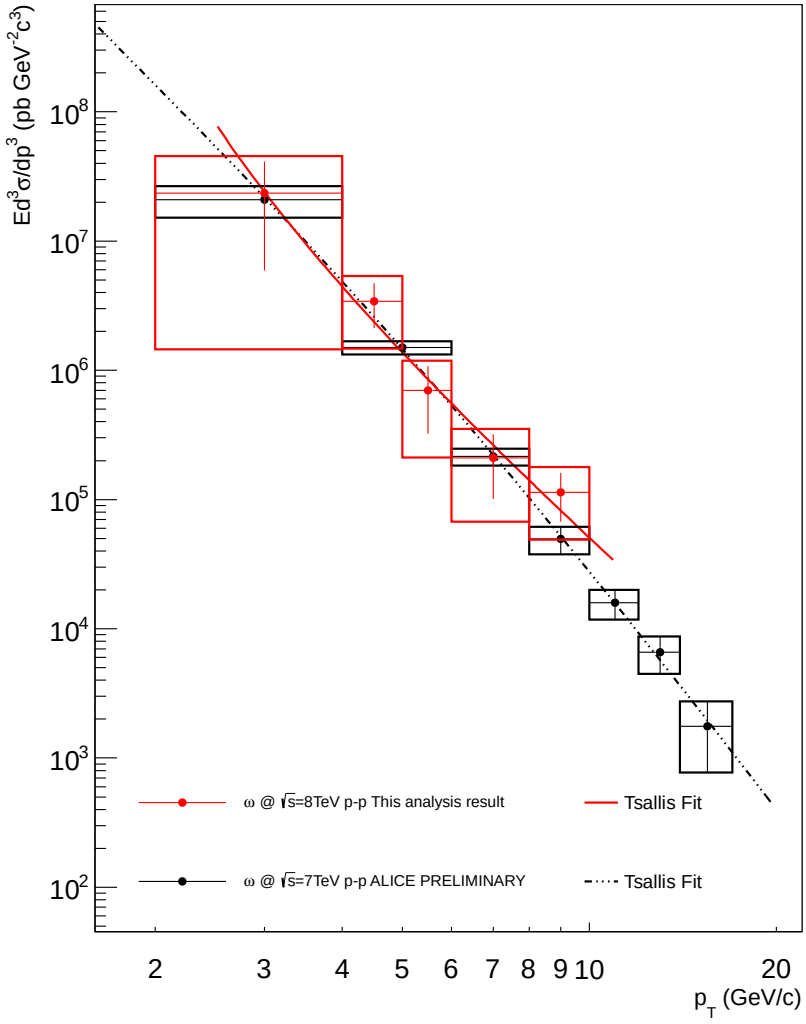

Figure 47: The $\omega \to 3\pi$ cross sections of different collisions energies. Red: 8TeV. Black: 7TeV. 7 TeV result is the ALICE preliminary.

5.2 Comparison with PYTHIA

The π^0 cross section is compared with PYTHIA[16][17]. Top plots in Fig49 shows you this analysis result (red) and PYTHIA result (black). The PYTHIA plots are fitted with Tsallis function and fit result is black line. The ratio of data to PYTHIA fit result is shown in bottom of Fig.49. Within the margin of uncertainty, the real data result is consistent with PYTHIA result. However, systematically, the real data result is somewhat larger than PYTHIA result. The measurement of neutral meson cross section in proton-proton collisions at 8 TeV is first time, so we should tune the simulation parameters .

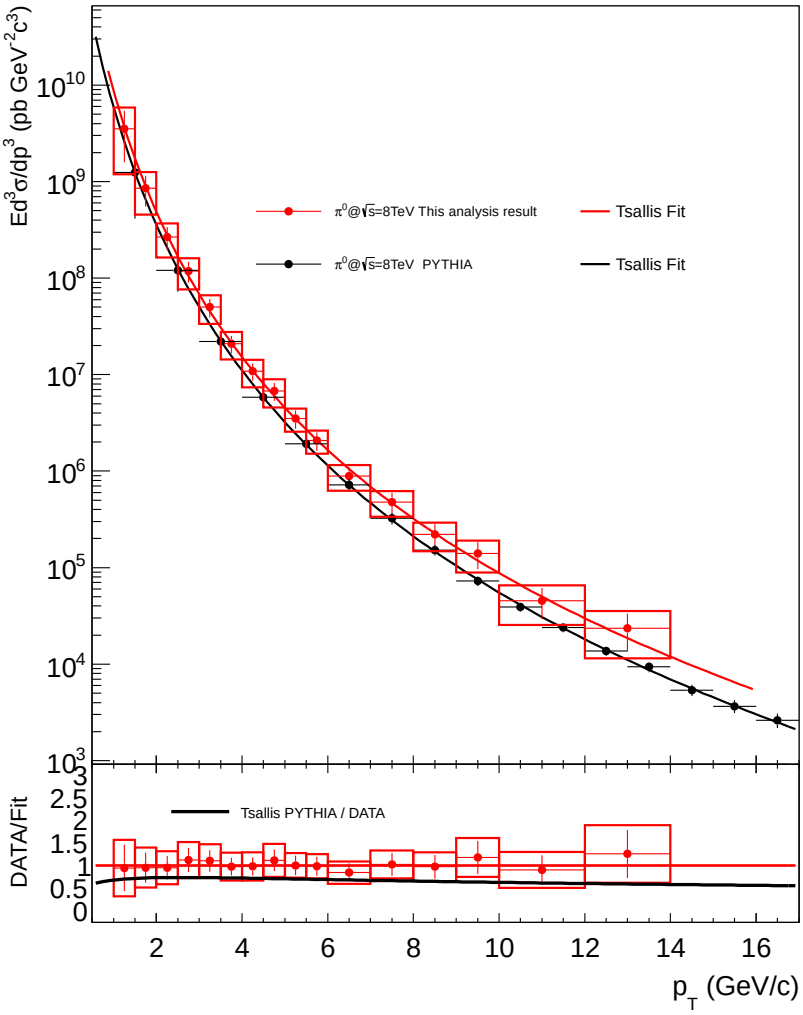

Figure 48: Top: Comparison between data and PYTHIA[16][17] 8 TeV result. The black line is Tsallis function fitted for PYTHIA 8 TeV. Bottom: The ratio of PYTHIA fitting function to data real data plots [4]

6 Conclusions

We have measured the invariant cross section of π^0, η and ω mesons with the PHOS trigger in proton-proton collisions at $\sqrt{s} = 8$TeV. The goal of this analysis is to measure three mesons invariant cross sections, to establish the method of estimating the trigger efficiency, and to provide reference data as a baseline of nucleus-nucleus and/or nucleus-proton collisions.

We obtained the invariant mass spectra via $\pi^0/\eta \rightarrow 2\gamma$ and $\omega \rightarrow 3\pi$ decay channels. We observed all 24 TRU response for clusters as a function of cluster energy. And then, we simulated these TRU response and became successful to estimate the trigger efficiency for π^0, η and ω mesons. The cross sections of π^0, η and ω mesons in proton-proton collisions at 8 TeV were measured and this measurement is first time in the world.

In this thesis, we analyzed 1.6 million PHOS triggered events and this is corresponding to 1.8 nb^{-1}, and the ALICE took about more than 1000 nb^{-1} PHOS triggered data in proton-proton collisions at 8TeV in 2012. We can analyze these data with the method I established and measure much higher p_{T} region. This study will contribute not only proton-proton collisions but also nucleus-nucleus and nucleus-proton collisions.

Aknowledgements

Among the ALICE Japan group, I thank Prof. T.Sugitate for helming us Hiroshima ALICE group and gave me the opportunity to present my analysis at ATHIC2012. I greatly thank Prof. K.Shigaki who supported not only my academic life but also private life. I acknowledge that he endorsed my stay at CERN and Quark Matter 2012. My experience there were wonderful and will be sustenance for my academic life. I would like to appreciate to Dr. K.Homma for teaching me attitude to the physics. Dr. H.Torii taught me many techniques for analysis. This analysis has finished with his techniques. Mr Y.Nakamiya. Dr. K.M.Kijima and Mr. H.Obayashi were peers in same room and they taught me not just the physics and cheered me sometimes. Junior fellows gave me a fun time, so I continued to research. I thank CNS members, especially, Mr. T.Tsuji and Mr. S.Hayashi. They supported my stay at CERN. I would like to express gratitude to my friends. My university life was very bright.

I must acknowledge PWGGA and PHOS offline analysis group members, especially, Dr. Y.Kharlov, Dr. V.Ryabov, Dr. D.Pressounko and Dr. C.Loizides. They gave me very important information for this analysis in a meeting and also many comments other than a meeting.

References

[1] The ALICE Collaboration, JINST 3, S08002 (2008).

[2] J.D. Bjorken, Phys. Rev. D 27, 140 (1983).

[3] M.Ouchida (Hiroshima University), "Production of Omega Mesons in Au+Au collisions at $\sqrt{s_{NN}}$ = 200GeV", Doctral thesis (2012).

[4] The ALICE colaboration, Phys.Lett.B 717 (2012).

[5] C. Tsallis, J. Statist. Phys. 52, 479-487 (1988).

[6] J. Wiechula, for the ALICE TPC Collaboration, Nucl. Phys. G: Nucl. Part. Phys. 38 (2011).

[7] F. Karsch, PoSCPOD 07, (2007) 026.

[8] LHCwebsite, http://lhc-statistics.web.cern.ch/lhc-statistics/

[9] The TOTEM Collaboration, CERN-PH-EP-2012-354.

[10] The PHENIX Collaboration, Phys. Rev. Ltte 101 (2008).

[11] The ALICE Collaboration, Technical Report, ALICE-DOC-2004-001 v.2 (2004) .

[12] L.Liu (University of Bergen), "L0/L1 trigger generation by the ALICE", Doctral thesis (2011).

[13] The ALICE Collaboration Preliminary, Quark Matter 2012, "Neutral meson production in pp and Pb-Pb collisions at the LHC measured with ALICE" .

[14] J.Midori (Hiroshima University), "Study of neutral mesons with the PHOS triggered data in proton-proton collisions at $\sqrt{s}$ = $7TeV$ ", Master thesis.

[15] PHENIX Collaboration, Phys. Rev. D 76, (2007).

[16] T.Sjostrand, Computer Physics Communication 135 (2001) 238-259.

[17] P.Skands, arXiv:0905.3418 (2009).

[18] R.Glauber, Nucl. Phys. B21 pp. 135-157 (1970).